UTILIZING A NEW CHEMILUMINESCENCE DIAGNOSTIC TO MEASURE

LAMINAR FLAME SPEED FROM SPHERICALLY EXPANDING FLAMES

A Thesis

by

MATTIAS ABRAM TURNER

Submitted to the Office of Graduate and Professional Studies of
Texas A&M University
in partial fulfillment of the requirements for the degree of

MASTER OF SCIENCE

Chair of Committee,	Eric L. Petersen
Committee Members,	Waruna D. Kulatilaka
	Chad V. Mashuga
Head of Department,	Andreas A. Polycarpou

May 2019

Major Subject: Mechanical Engineering

ABSTRACT

Laminar flame speed provides a metric by which to evaluate chemical kinetics models, which are used to predict the complex behaviors of combustion processes. Historically, the schlieren technique has been used in the spherically expanding, optically tracked flame rig to measure laminar flame speed, but this experimental method only produces laminar flame speed data.

Chemiluminescence of intermediate radicals is indicative of the high-temperature reaction zone of the flame, and it can be used to measure laminar flame speed in a similar fashion to the widely used schlieren imaging technique while also measuring other species-specific data to be used for model validation. An experimental study of laminar flame speed of spherically expanding methane-air flames measured from chemiluminescence of OH* at 306 nm and of CH* at 430 nm is presented for the first time.

To validate the new diagnostic and compare to existing data in the literature, flame speeds for one atmosphere and room temperature methane-air flames were measured from OH* and CH* chemiluminescence for equivalence ratios from 0.7 to 1.3. There was no significant difference between flame speeds measured from different wavelengths (or species) of chemiluminescence. The new data are in good agreement with data from the literature, indicating that chemiluminescence can be used to extract accurate laminar flame speed measurements from spherically expanding flames.

Additionally, a set of experiments was performed that took advantage of the window arrangement of the facility by simultaneously capturing schlieren images and chemiluminescence images of each experiment. This set of flame speed data showed that, within the uncertainty of the chemiluminescence measurements, there was no difference between the flame speed measured using schlieren and that measured using chemiluminescence.

Another set of experiments was conducted for mixtures of methane, oxygen, and carbon dioxide in the interest of studying oxy-methane combustion for supercritical carbon dioxide power cycles. These tests showed good agreement with existing data. Future improvements to the chemiluminescence technique can be made, specifically with respect to image quality and noise reduction.

ACKNOWLEDGMENTS

CONTRIBUTORS AND FUNDING SOURCES

Contributors

This work was supervised by a thesis committee consisting of committee chair Dr. Eric L. Petersen and committee members Dr. Waruna D. Kulatilaka of the Department of Mechanical Engineering and Dr. Chad V. Mashuga of the Department of Chemical Engineering.

The machining of the window plugs and the optical fiber adapter was completed by the student with guidance from Carl Johnson, Turbomachinery Laboratory facility manager.

The setup and operation of the chemiluminescence diagnostic and the execution of the flame speed tests were performed with assistance from Tyler Paschal and Kyle Ruehle. The flame images were processed using the edge-detection code written by Travis Sikes.

All other work conducted for the thesis was completed by the student independently.

Funding Sources

TABLE OF CONTENTS

LIST OF FIGURES

LIST OF TABLES

1. INTRODUCTION

Laminar flame speed is a fundamental property of flammable mixtures that is dependent on a number of physical parameters, and is defined as the rate at which an unstretched, smooth, adiabatic, 1-D, planar flame front propagates through a flammable mixture [1-3]. The utility of laminar flame speed stems from our ability to determine this property both theoretically, by solving both the full chemical kinetics and the 1-D fluid mechanics of the system, and experimentally, typically through laboratory observation of a stretched laminar flame. A comparison of the calculated value to the experimentally measured value provides the combustion community with a direct metric for validating theoretical prediction methods.

Experimentally, laminar flame speed is measured by several methods, each with its own advantages, drawbacks, data acquisition systems, and necessary correction techniques. The experimental facility employed in the author's laboratory at TAMU is a recently installed spherical flame type rig, which benefits from the high level of control over the conditions of each experiment, the lack of initial flow instabilities in laminar flame tests, and a well-established flame stretch correction. The facility uses a schlieren optical diagnostic, where the density gradient caused by the flame is recorded to produce a series of images that are then used to calculate the rate of growth of the flame. This type of facility and optical tracking method has been used in the author's laboratory for over a decade [4-14].

Currently, schlieren imaging produces a single type of quantitative data from these spherical flame tests: laminar flame speed. While the method works well, there is another optical diagnostic based on chemiluminescence that has been used historically in other flame rig types for species-specific measurements. Chemiluminescence has been used in spherical flame type apparatuses before, for example by Dandy and Vosen [15], but it has yet to be adapted for the purpose of measuring laminar flame speed in a constant-volume, spherical flame type rig.

Chemiluminescence is shown herein to provide accurate laminar flame speed measurements from spherically expanding flames. Methane-air flames at one atmosphere and room temperature were chosen as the mixture and conditions with which to validate the new diagnostic due to the large body of literature with which to compare the flame speed values determined from chemiluminescence. Taking advantage of the additional optical access offered by the recently developed flame speed facility in the author's laboratory, the chemiluminescence system was installed concurrently with the existing schlieren diagnostic and both systems were used simultaneously to directly compare the two optical techniques. Additionally, in the interest of expanding the understanding of supercritical carbon dioxide combustion as it applies to gas turbine power generation cycles, the chemiluminescence system was used to measure flame speeds of oxy-methane flames diluted with carbon dioxide.

Chapter 2 provides a background overview of the optically tracked, spherically expanding flame experiment, the existing schlieren technique, and the advantages of developing a chemiluminescence diagnostic for laminar flame speed measurements. A

description of the constant-volume spherical flame rig and the optical diagnostics is given in Chapter 3. In Chapter 4, the current laminar flame data processing method is described. Chapter 5 presents the experimental results and discusses their relevance. Concluding remarks and future work are given in Chapter 6.

2. BACKGROUND

There are several experimental methods for measuring laminar flame speed, including heat flux, Bunsen burner, counterflow, and spherically expanding, among others. To produce laminar flame speed data from the experiment, some methods use heat transfer, pressure rise, or the system flow rate, while others use an optical technique. The spherically expanding flame experiment is one such example of an experiment that relies on optical access to extract laminar flame speed from the experiment. In this type of experiment, a constant-volume vessel is filled with the fuel-oxidizer mixture of interest, and the mixture is subsequently ignited. This type of experimental apparatus holds a strong position in the field of combustion research due to its unique ability to achieve engine-relevant conditions [12, 16]. Through a set of windows, the propagation of the flame is recorded using a high-speed camera. The existing optical diagnostic uses a technique that highlights the schlieren caused by the large density gradient at the leading edge of the flame. Schlieren are visual artifacts of the change in the index of refraction of the gas mixture that results from the combustion reaction. A collimated beam of light is passed through the vessel and focused onto the high-speed camera sensor. Schlieren imaging has been used successfully as a combustion and fluid mechanics diagnostic for decades [17]. Sample images of spherical flame schlieren recorded in the author's facility are given in Fig. 1.

While there are many visually interesting characteristics of flames that can be seen in flames using a schlieren setup, such as wrinkling and the onset of thermal-

diffusive flame instabilities, the technique is currently limited to producing only laminar flame speed data. Schlieren provides no information about the distribution or concentration of chemical species in the flame. However, a chemiluminescence diagnostic produces exactly that, while also providing data with which to measure laminar flame speed.
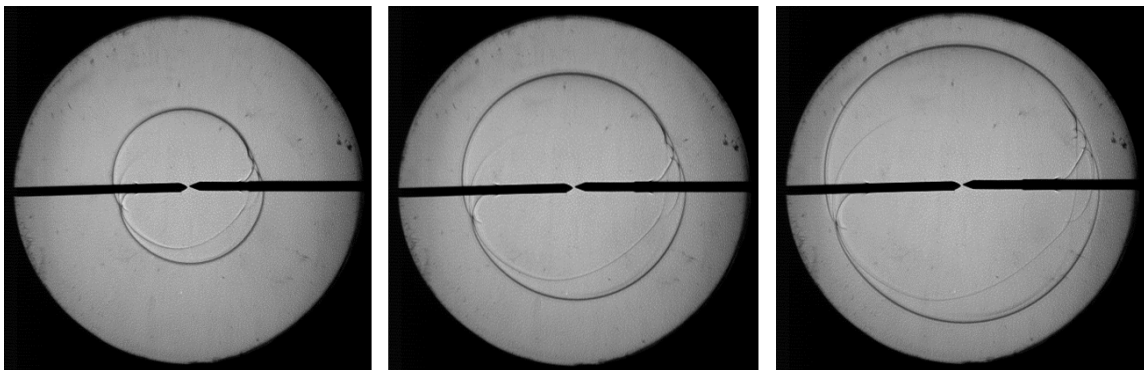
Figure 1: Sample images of flame schlieren recorded in the author's laboratory. The dark lines across the center of the images are the electrode and rods used to generate the spark used for ignition.

Chemiluminescence has been used as a combustion diagnostic since the beginning of combustion research because it is an obvious indication of a combustion reaction that can be seen with the naked eye. Studies that relate chemiluminescence to chemical kinetics modelling date back to at least the 1920s [18-20]. Chemiluminescence occurs because a portion of the population of intermediate species in the reaction, which have lifetimes on the order of microseconds [19, 21], has absorbed sufficient energy to become electronically excited, and photons are emitted during the relaxation of the excited species, which have even shorter lifetimes on the order of tens of nanoseconds

[19], back to the ground state. This emission is known as chemiluminescence, and it can be traced back to individual species based on the characteristics of the emission, allowing for time-resolved chemiluminescence photography in the laboratory. Every excited species has characteristic emission spectra that can be isolated and recorded through an optical diagnostic. Common species that are targeted for this type of observation of flames are the excited hydroxyl radical OH* and the excited methylidyne radical CH*, although there are others, like C_2 [22]. These radicals are chosen because of their ubiquity in combustion reactions, particularly in air-breathing, hydrocarbon-fueled applications. Sample images of spherical flame chemiluminescence recorded in the author's facility using the new optical diagnostic are given in Fig. 2. As is detailed herein, the chemiluminescence images are similar to the schlieren images, allowing the existing schlieren image analysis process to be adapted for the chemiluminescence images with relative simplicity.
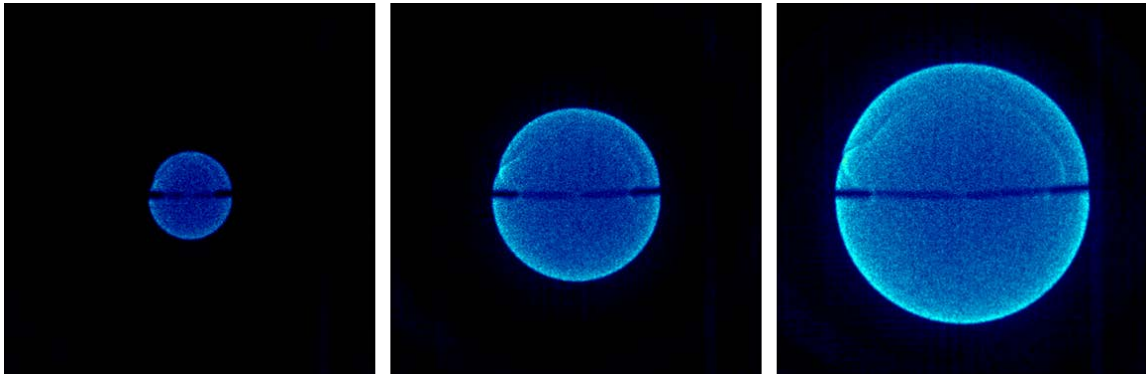
Figure 2: Sample images of spherical flame chemiluminescence emitted from CH* at a wavelength of 430 nm recorded in the author's laboratory. The blue color is the default color scale in the recording software, and is used for presentation purposes only.

The emission spectra from each species are unique and contain wavelengths of infrared, visible, and ultraviolet light. Because certain spectral lines are unique to certain excited species, it is possible to image those species by blocking out all other light through the use of a narrow bandpass optical filter that allows transmission of only the target wavelength and a narrow band around the target. For the radicals used in this work, namely OH* and CH*, the unique spectral lines fall in the ultraviolet region. For OH* and CH*, emission at 306 nm and 430 nm, respectively, was chosen.

Chemiluminescence has been used to provide useful species concentration data that can be linked to important combustion parameters, such as measurements of local equivalence ratio [22-25] and heat release rate [25, 26], as well as spatially resolving different zones of the flame, like the preheat zone, reaction zone, and recombination zone [1, 2]. The species spatial gradients in a flame are also key markers of flame characteristics like the temperature gradient and the heat release gradient, and provide information that can be used to validate chemical kinetics models.

A chemiluminescence diagnostic provides combustion researchers with a wide variety of useful species-specific data, and a schlieren diagnostic provides laminar flame speed data. However, in the laboratory it is typically not practical to have multiple diagnostics set up simultaneously for one experimental facility, unless the facility has been designed for such a configuration. Even then, there remains the time and effort required for operation of the diagnostic systems and the subsequent data analysis. If a single diagnostic system capturing a single set of data can be applied to the extraction of multiple streams of information, then for practical purposes it is valuable to develop

such a diagnostic. This thesis serves to experimentally validate the development of a new chemiluminescence diagnostic for the purpose of measuring laminar flame speed in the spherically expanding flame facility at Texas A&M University.

3. EXPERIMENTAL FLAME FACILITY AND NEW CHEMILUMINESCENCE IMAGING SYSTEM

In this Section, the constant-volume, cylindrical vessel in the author's laboratory is described first, followed by a detailed explanation of the new chemiluminescence imaging setup. Some of the material herein is reprinted from Turner et al [27] with permission from AIAA.

3.1. TAMU's Turbulent Flame Speed Vessel (TFSV)

The experimental apparatus employed for this work is a fan-stirred flame vessel, known as the Turbulent Flame Speed Vessel (TFSV), and is designed for initial conditions of up to 10 bar and 400 K. The initial pressure condition is limited by the strength of the quartz windows of the vessel, and the initial temperature condition is limited by the O-rings currently used to seal the vessel. The apparatus is shown in Fig. 3 and is described more fully by Morones et al. [11, 12]. The vessel is a constant-volume, stainless steel cylindrical vessel with four, 127-mm (6 in) diameter optical ports, each installed with 88.9-mm-thick (3.5 in) fused quartz windows to provide two perpendicular axes of optical access. To minimize the exposure of the quartz windows to the violent and potentially damaging combustion events, only the windows used for the optical access required by the particular optical diagnostic are installed in the vessel during flame testing. For example, the schlieren diagnostic requires two windows along a single axis, while the chemiluminescence diagnostic requires only one window. The facility has

also been used for planar laser induced fluorescence (PLIF) imaging, for which two windows on perpendicular axes were required [28]. The unused optical access ports are instead plugged with aluminum round stock, machined in-house to match the dimensions and tolerances of the windows. The rig also possesses four stirring motors positioned tetrahedrally with impellers to provide turbulence generation when desired. Laminar tests can be conducted with the fans installed in the vessel.

Figure 3: Turbulent Flame Speed Vessel (TFSV), with two upper stirring motors visible at top and two optical ports visible with quartz windows installed.

The vessel is also outfitted with a thermocouple, to measure the initial temperature of test mixtures, and with a pressure transducer, to measure the pressure rise in the vessel during an experiment. The pressure data are important, as the constant-volume conditions mandate an increase in system pressure with an increase in temperature. Previous studies in this rig have shown that the pressure rise in the unburned gases is negligible for the time that the flame is visible through the vessel windows [12]. This means that the assumption of constant pressure remains valid long enough for useful data to be collected. In any case, nonideal flame behavior, such as an increase in pressure due to confinement, is clearly visible during the data analysis process, which is discussed in Chapter 4.

A schematic of the existing schlieren diagnostic from a top-down view is provided in Fig. 4. It is a modified Z-type setup, with lenses used to collimate the light and flat mirrors used to direct the collimated light through the vessel. The diffracted light is blocked by the circular knife-edge, or iris diaphragm, located directly in front of the camera. The camera used here is a Photron Fastcam SA1.1, set at 2000 frames per second for this study.

The vessel and all necessary diagnostics are located in a small room built into the main laboratory test cell. This smaller room, known as the blast room, has cinderblock and concrete walls reinforced with steel rebar and is accessible through a locking blast door. The blast room and the main test cell are evacuated immediately prior to each flame test to ensure the safety of lab personnel in the event of a catastrophic vessel failure.
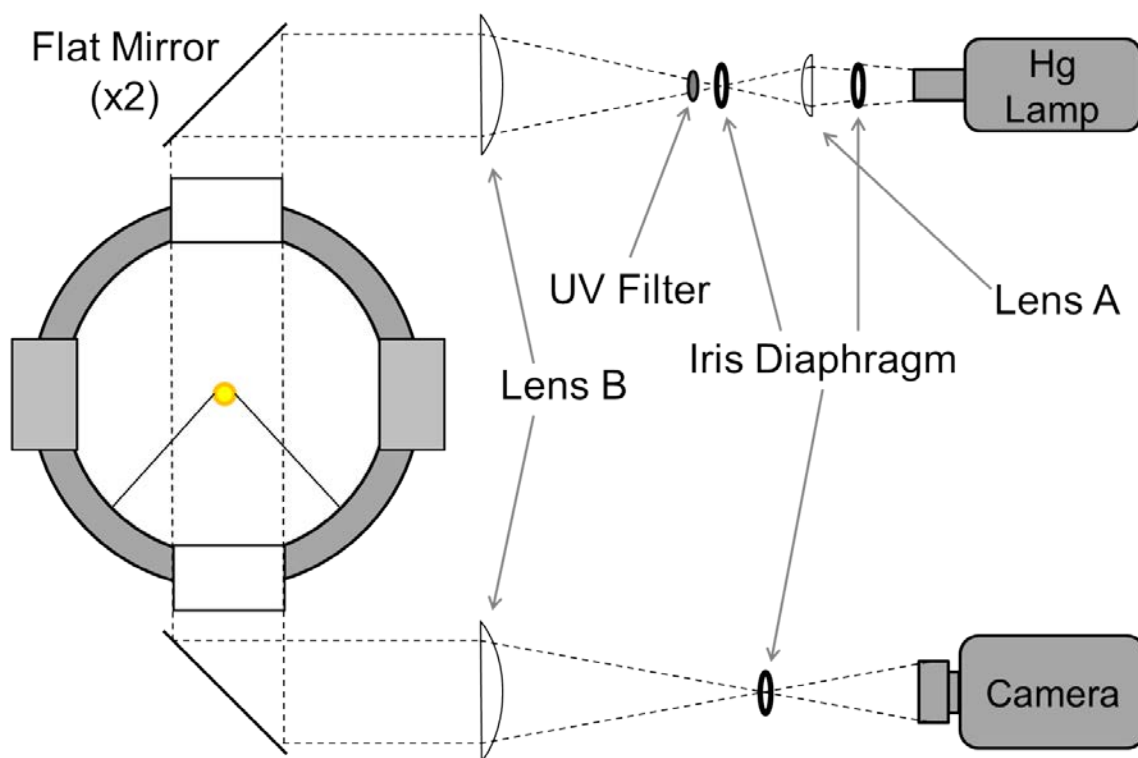
Lens A: Plano-convex, ⌀50.8 mm, f = 100 mm
Lens B: Plano-convex, ⌀200 mm, f = 800 mm

Figure 4: Top-down schematic of schlieren optical setup.

Gas mixtures were prepared using the partial pressure method, by which each constituent gas in the reactant mixture was added to the vessel in ascending order of partial pressure. All gases used in this study were ultra-high-purity grade and sourced from Praxair. Before filling the vessel with the reactant mixture, the vessel was evacuated using a roughing pump to a pressure below 0.3 torr. This residual gas is assumed to be air. The vessel was then filled with each gas in ascending order of partial pressure. During the filling process, the temperature of the gases in the vessel was

monitored using a thermocouple. The temperature of the gas mixture was allowed to return to within 0.2 K of the initial temperature of the mixture before the next component was added. The filling manifold is effectively the same as described by previous TAMU researchers, for example Sikes [9].

Reactant mixtures are ignited using an automotive ignition coil connected to an electrode, the tip of which is located very near the center of the volume of the vessel. A grounding rod of similar shape and size to the electrode rod is positioned such that the gap between the tip of the grounding rod and the tip of the electrode is as close to the center of the volume of the vessel as possible, as can be seen in the schlieren images in Fig. 1. This alignment is crucial to ensuring that the flame growth begins at the center of the vessel, so that the flame is visible through the windows for the longest possible time. The gap ideally is as small as possible to minimize the amount of energy added to the gas beyond what is needed to ignite the mixture, and therefore is on the order of 1-3 millimeters. The spark is created by supplying the ignition coil with a 12-volt power circuit and a normally open, 5-volt triggering circuit. When the 5-volt circuit is closed, typically by the press of a button that initiates a triggering process, the coil discharges and the spark is generated.

Any triggering system for the facility relies on a normally open ignition switch or button located outside the blast room. This button, when pressed, closes the 5-volt ignition triggering circuit and initiates both the ignition and the data acquisition. The source of the 5-volt trigger voltage can be configured differently for different imaging systems. For the schlieren imaging system, a dedicated power supply is used to generate

13

both a 12-volt source to power the ignition coil and a 5-volt source to power the triggering circuit. When the ignition button is pressed, the 5-volt signal is applied to both the ignition coil, generating the spark, and the trigger input to the high-speed camera, initiating image recording. With these schlieren tests it is not crucial to temporally resolve the occurrence of the spark and the beginning of image recording, because the camera can be configured to save a large number of frames before and after the arrival of the trigger signal. From there it is a simple matter to play back the recorded images to locate the useful images of flame propagation. This procedure for is in contrast with the chemiluminescence setup, where temporal resolution of the spark and the start of image recording must be known before each test. This modified procedure is described in Chapter 3.2.

3.2. New Chemiluminescence Imaging System

The optical setup was comprised of a Photron SA-Z high-speed camera coupled to a LaVision High-Speed Intensified Relay Optics (HS-IRO) unit and is described in more detail by Paschal et al. [28]. The timing and triggering of the system relied on a delay generator, while the gating settings for the camera and HS-IRO were controlled using the LaVision software DaVis and the accompanying IRO Controller and PTU-X. For all the laminar experiments conducted in this study, the frame rate of the system was set at 2000 frames per second. A UV-grade lens was used to focus the emission of the flame into the HS-IRO and increase the viewable region of the interior of the vessel. The camera and HS-IRO were positioned such that the focal length of the lens landed just

beyond the spark gap, i.e. the center of the vessel. The system was focused by placing an image or business card with a clearly defined pattern at the center of the vessel, perpendicular to the optical axis.

To isolate the desired wavelength for each of the radicals, Semrock Brightline single-band bandpass optical filters were installed in front of the intensifier. The filter used for OH* was 315 nm ±15 nm, and the CH* filter was 434 nm ±17 nm. Broadband emission was also recorded for each equivalence ratio for emission between the wavelengths of approximately 200 nm and 400 nm. Because the emission of the OH* and CH* radicals at the chosen wavelengths is relatively weak, the light must be amplified by the HS-IRO to raise the intensity of the captured emission to a level that is within the useful range of the sensor of the camera. This amplification can be adjusted manually with the gain setting in the LaVision DaVis software. Adjusting the gain setting also allowed the relative level of brightness of the images to be maintained over the range of equivalence ratios. The range of gain values used for this work ranged from 40% to 63% on the internal scale set by the intensifier software. This range of values was determined by conducting preliminary tests at the equivalence ratios corresponding to the lowest and highest flame speeds, which produced the upper and lower bounds on the gain setting, respectively. The gain values for the remaining tests were found by interpolation. In general, the broadband tests required the least amount of gain, whereas the CH* tests required the most amount of gain. Because the gain was changed for each test, inferences cannot be made regarding the relative quantity of CH* or OH* generated in the flame. Of course, the gain must be kept constant between runs to make any

quantitative comparisons in that regard. The matrix of settings for the camera and HS-IRO for the laminar methane-air flame tests are tabulated in Table 1.

Table 1: Matrix of settings for the camera and HS-IRO for each species of chemiluminescence.

Species Type	Frame Rate (fps)	Gain (%)	Gate Width (μs)	Filter Wavelength (nm)
OH*	2000	47-57	65	315 ± 15 nm
CH*	2000	53-63	65	434 ± 17 nm
Broadband	2000	40-52	65	200-700 nm

The intensifier is a sensitive instrument and must be protected from high-intensity light, including the emission from the spark at the very beginning of the test and emission from the flame near the end of the experiment. Repeated overexposure of the IRO can cause damage, so a triggering and timing system was designed to prevent the exposure of the IRO to the spark emission and the intense late-flame emission. The initial version of this triggering system, depicted by the schematic in Fig. 5, relied on a photodiode (PD) to detect the flash of the spark and generate a signal to begin the triggering timeline. One of the unoccupied ports of the vessel was outfitted with a small, windowed adapter inside which a fiber optic cable was fixed. The adapter was machined and assembled in-house by the student. The optical fiber transmitted the spark emission from the vessel wall to a photodiode. The photodiode then emitted a voltage that triggered the delay generator and began the experiment timeline.
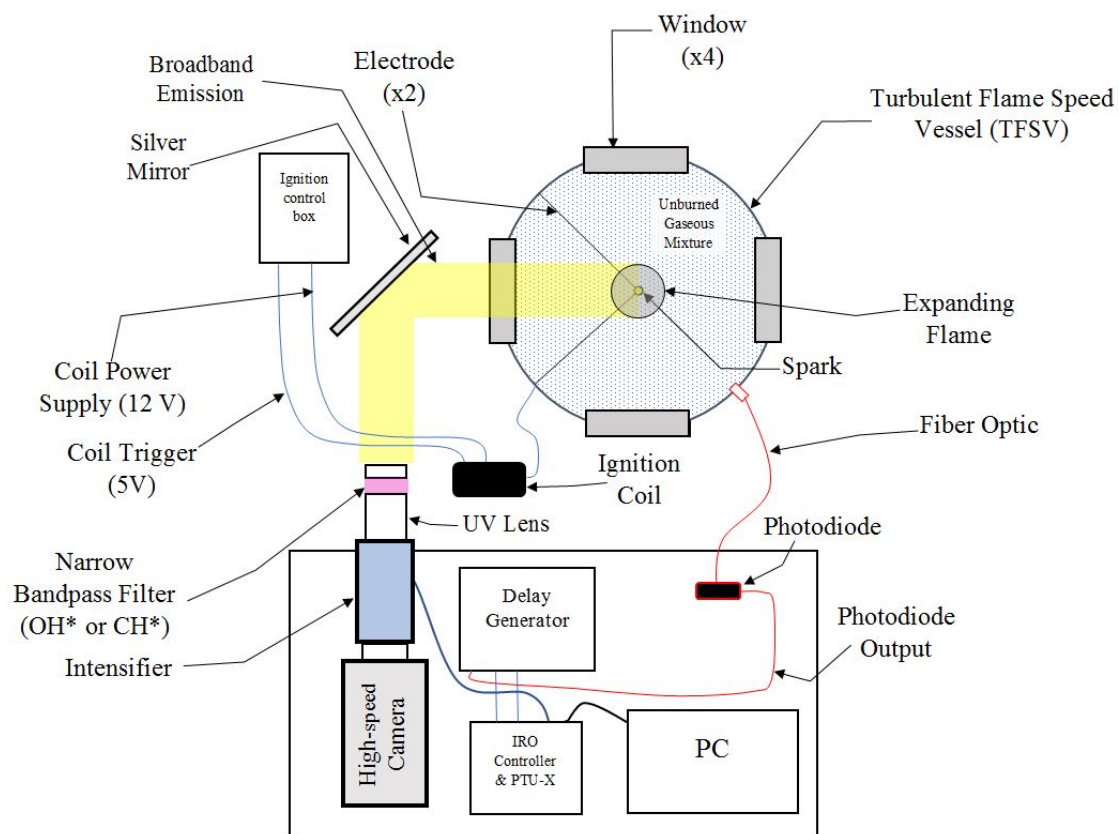
Figure 5: Schematic of first iteration of triggering system, with the optical fiber and photodiode shown in red. Ignition button not shown.

A representative plot of photodiode response to a real flame test is shown in Fig. 6, on the left. The spike in voltage at time zero is due to the spark and is shown in detail on the right side of Fig. 6. The subsequent rise in voltage is due to the emission from the flame. The flame grows to the edge of the viewing windows within 100 ms of the spark, meaning that the flame can be imaged safely well before the late-flame emission becomes too intense for the intensifier. Unfortunately, the voltage spike seen in Fig. 6 at time zero was not typical. In most cases the spark emission could not be distinguished from the noise in the signal. This photodiode-based system proved to be inconsistent, as

the intensity of the spark varied between tests and the fiber alignment with the spark location could not be reliably determined. This configuration yielded approximately 40% repeatability: the diode would not always detect the spark, and the imaging system would not trigger until the already-propagating flame was intense enough to be detected by the photodiode. This first iteration for the timing sequence exposed the intensifier to the late-flame events, and was quickly discontinued in favor of a successfully reliable system.
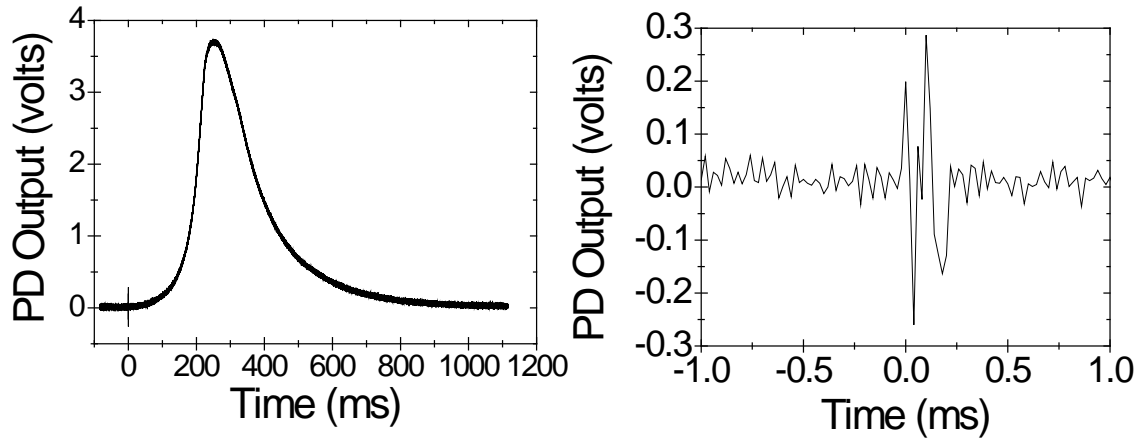
Figure 6: Left: Plot of photodiode voltage output from a real flame test. Voltage spike due to spark emission can be seen at time zero. Right: Close-up of voltage spike from spark emission.

The final triggering system, shown by the schematic in Fig. 7, used the 5-volt ignition coil trigger signal as its time-zero master trigger. The photodiode and optical fiber were removed, and the input to the delay generator was instead connected to the 5-volt trigger source of the ignition coil, shown in Fig. 7 as the green line exiting the ignition control box. All other hardware remained the same. Over the course of this

work, this "hard-wired" triggering system had 100% repeatability, and never failed to trigger on-time.
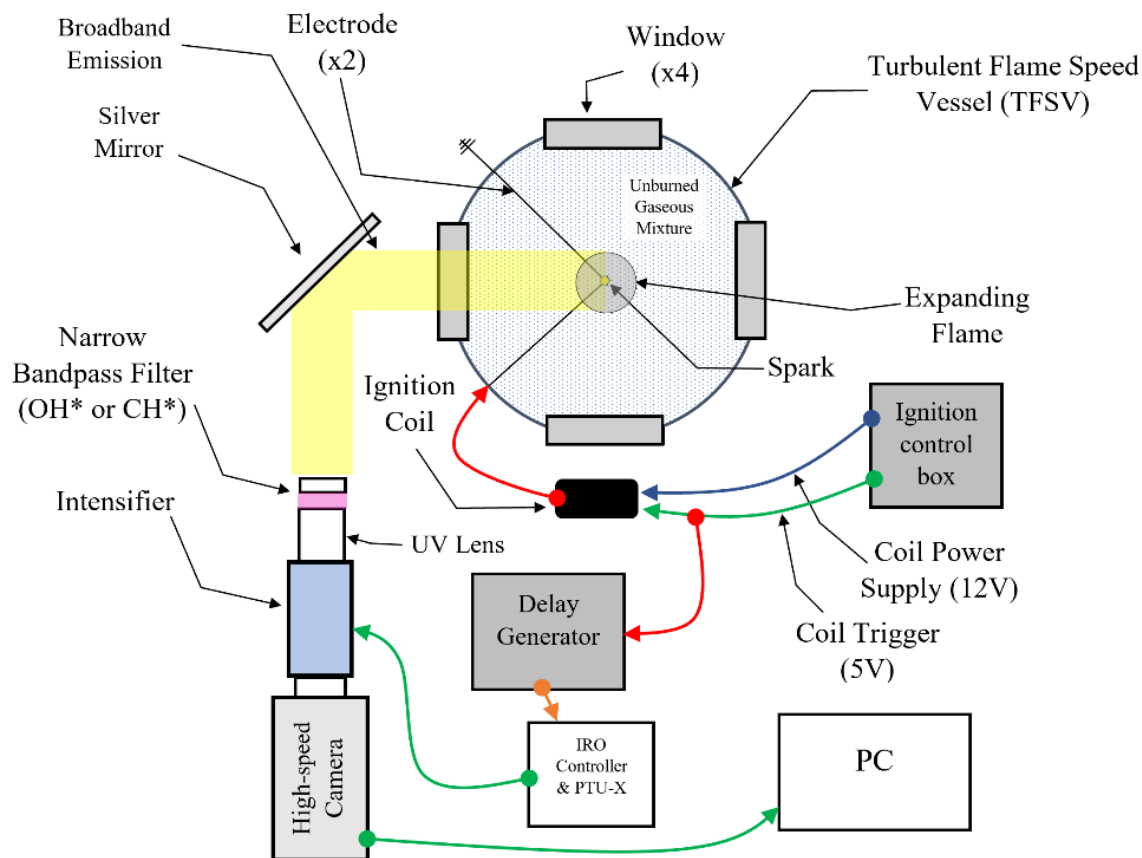
Figure 7: Schematic of hard-wired triggering system, with the delay generator input source changed to the 5-volt coil trigger signal.

Using this hard-wired triggering system, time-zero occurs before the spark is generated. Therefore, the opening of the HS-IRO shutter needed to be delayed by a short time to avoid exposing it to the spark emission. To determine this delay time, the vessel was opened and the photodiode placed inside at a safe distance from the spark gap. The GageScope data acquisition system and software were used to monitor and record the 5-

volt coil trigger signal and the photodiode response to the spark emission for a series of test sparks. This showed that the spark emission remains significantly intense for approximately 13.35 ms after the arrival of the 5-volt trigger, which was then used as the delay time at which the HS-IRO shutter was first triggered to open for each experiment. Although changing the size of the spark gap affected the magnitude of the intensity, the duration did not vary significantly with spark gap size.

In comparison to the spark emission, the late-flame emission is both greatly more intense and much simpler to avoid. Because the flame speed of the chosen test mixture was already known to the student from prior experience, it was a simple matter of calculating how much time was required for a flame to grow to a size larger than what is viewable through the window. Of course, this time depends on the equivalence ratio of the flame and had to be estimated for each equivalence ratio. This time was then added to the 13.35 ms of initial delay to produce the time at which the HS-IRO shutter needed to be closed.

Because the camera can only see what is sent through the HS-IRO, the camera was set to begin recording at time-zero and stop recording some time after the HS-IRO shutter had been closed. This meant that a small number of blank images were recorded before and after the useful data had been recorded, serving as a check to ensure that the HS-IRO did, in fact, open and close as expected.

For the set of experiments where schlieren imaging and OH* chemiluminescence imaging were conducted simultaneously, a schematic of the optical setup is given in Fig. 8. The schlieren optics were installed in their usual position, and the chemiluminescence

optics were moved to the other optical axis. The optics for the mercury arc lamp contain a visible bandpass filter that prevents UV light from contaminating the chemiluminescence diagnostic, as shown previously in Fig. 4. The ignition button, shown in red in Fig. 8, was used as the master trigger for both optical systems, providing time-synchronized sets of images from each diagnostic.
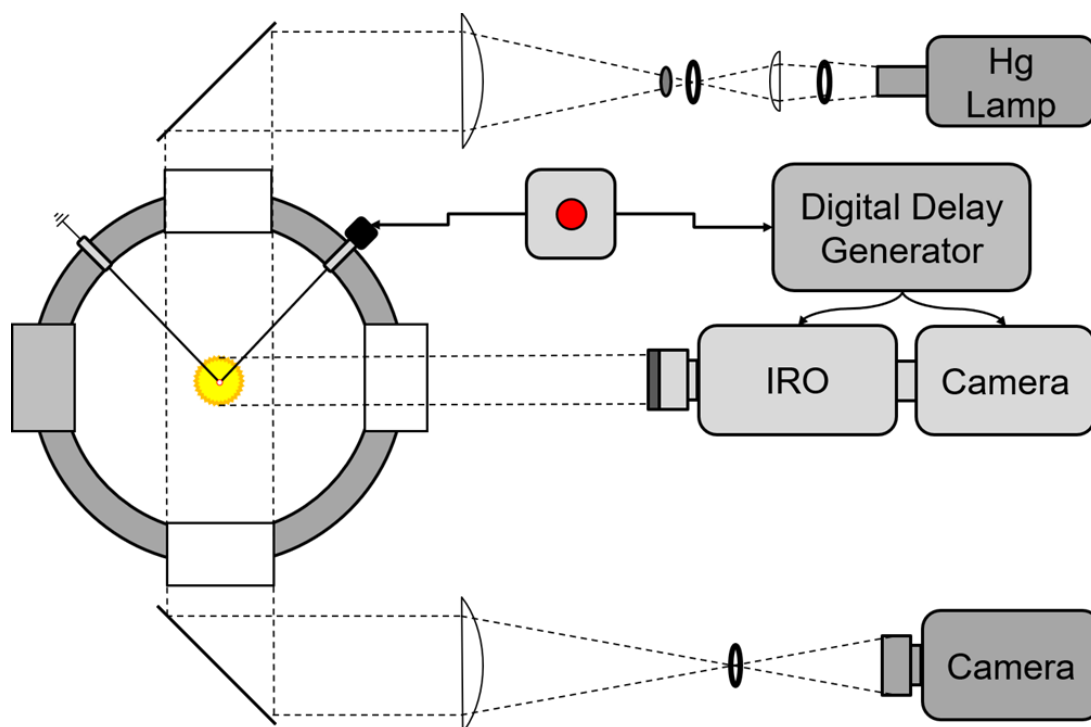
Figure 8: Schematic of simultaneous schlieren and chemiluminescence optical diagnostics with ignition button indicated in red.

4. LAMINAR FLAME SPEED DATA PROCESSING

The extraction of laminar flame speed from the flame images involves several steps, each of which are detailed in the following paragraphs. This process is effectively the same for the chemiluminescence images as for the schlieren images, but any differences between the two are described herein. First, the leading edge of the flame is detected in every image using a Matlab code developed in-house. A circle is fit to the detected edge and then, using the frame rate of the camera to determine the time interval between images, the growth of the radius of the flame is tracked as a function of time. The rate of the growth of the flame is then corrected for the effect of flame stretching and density changes to arrive at the reported laminar flame speed, S_L^0.

The image-processing algorithm requires image files to be in grayscale format. The schlieren images are output by the Photron SA1.1 camera in grayscale by default; however, the chemiluminescence images output by the LaVision DaVis software are not true grayscale, even when the grayscale option is selected in the software. To accommodate the chemiluminescence images and prepare them for analysis, a short Python script was written to convert the chemiluminescence images to grayscale and to simultaneously standardize the file naming convention.

The images, whether they are schlieren or chemiluminescence, are then processed using an edge-detection algorithm developed in-house, as described by Sikes [10]. For each image, the algorithm subtracts the intensity of each pixel from the intensity of the corresponding pixel of the previous image, thereby producing a new

"image" containing only the difference between two consecutive images. This difference in intensity shows the change in the position of the leading edge of the flame, which then provides a strong curve for edge detection. The edge detection process follows the methodology proposed by Canny [29].

A circle is fit to the leading edge of the flame in every image, providing the radius of the flame at known time intervals based on the frame rate of the camera. A series of chemiluminescence images from this study are shown in Fig. 9, with the raw images shown in the lower row and edge-fitting shown in the upper row.
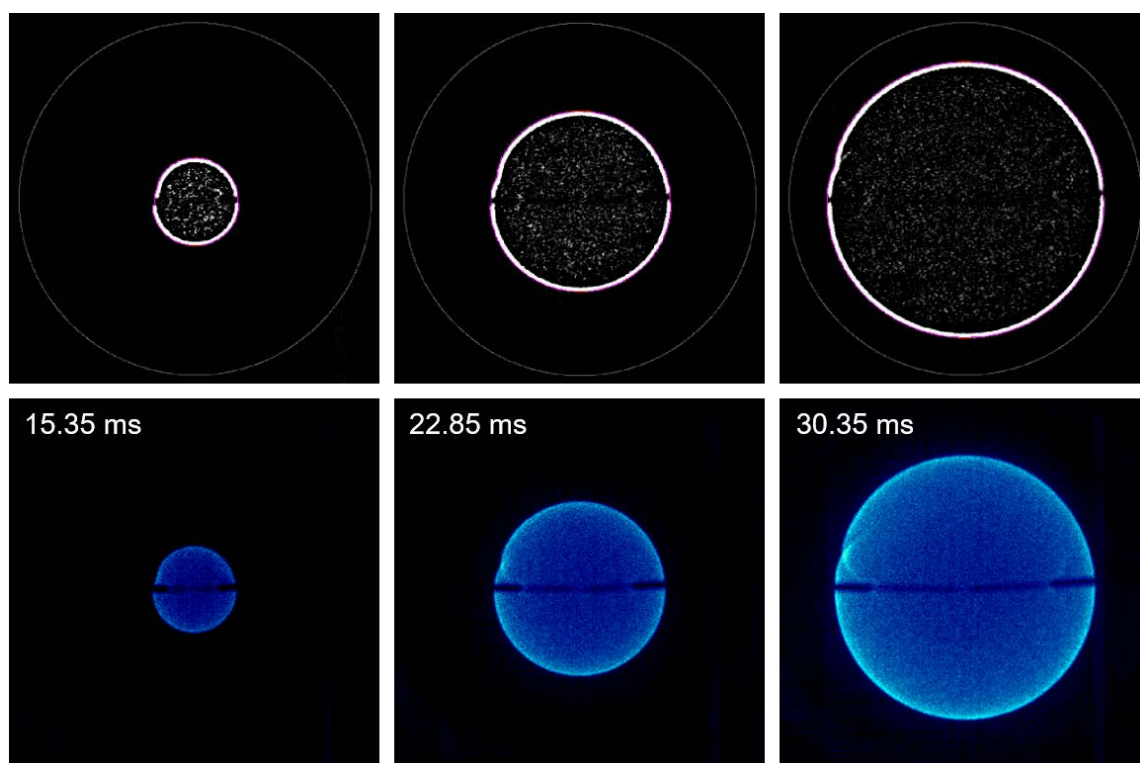
Figure 9: Progression of CH* chemiluminescence of a methane-air flame at an equivalence ratio of 1.1 with edge fitting shown in the upper row. Timestamp is relative to time-zero, as described in Chapter 3.

The first frame of each set of images is used to calculate the resolution of the images. This is relatively straightforward for the schlieren images, because the first frame is always chosen to be the frame before ignition; i.e., there is no flame in the first frame. This flameless frame is simply an image of the window of the vessel. The diameter of the window is known, which provides a scale with which to determine the real size of the flame in every image in centimeters.

The chemiluminescence images are not so simple: the first frame always contains the flame after it has grown for only 13.35 ms, which is to say that the flame is small. The code assumed this small flame to be the vessel window and subsequently produced nonsensical values for the flame radius. This problem was solved by using a copy of the final image of the flame in each chemiluminescence run as the first image, so that the largest visible flame (which has a diameter similar to that of the window) was used to determine the resolution of each image in pixels per centimeter. However, because the emission from the flame is not collimated, the diameter of the largest visible flame cannot be assumed to be equal to the diameter of the window, and a separate scale must be used. This additional scaling was achieved using a printed image with known dimensions, as shown in Fig. 10. The concentric circles on the left were printed at a scale that produced a line thickness of 0.25 inches. This printed image was placed at the center of the vessel, perpendicular to the optical axis of the camera, and then imaged with the camera and HS-IRO installed exactly as they would be for a chemiluminescence test. This image was also used to focus the camera. This procedure was repeated any time the camera and HS-IRO were moved.

24
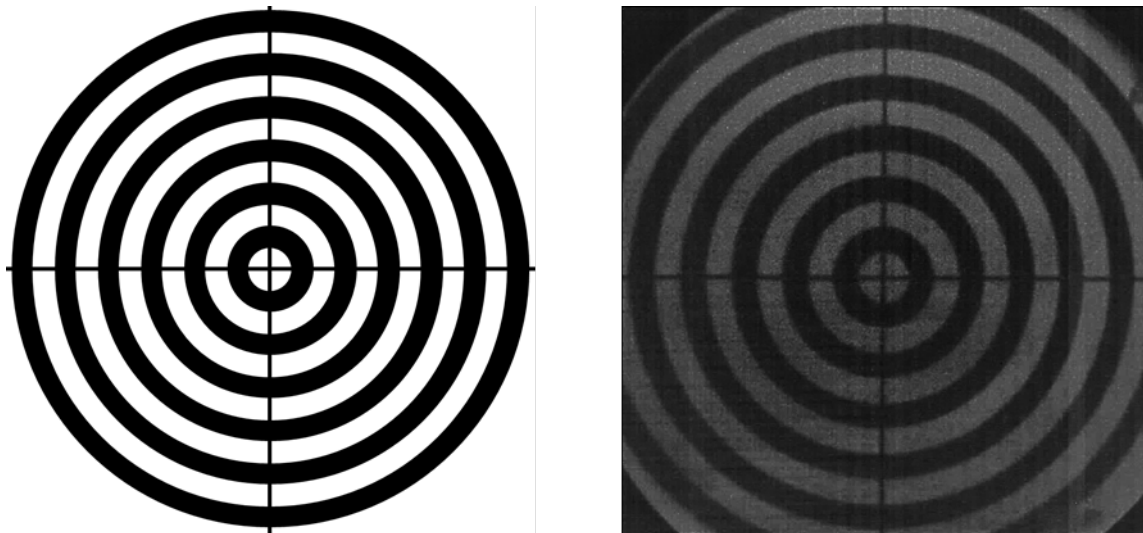
Figure 10: On left, the scale pattern used to determine resolution of chemiluminescence images. On right, an example image taken by the chemiluminescence imaging system during a resolution calibration.

This calibration process is the largest source of uncertainty in the chemiluminescence data. The resolution of the images is good; i.e. the camera sensor is large enough; but the edges of the pattern in the calibration images were never perfectly crisp. This is probably due to the lens in place on the HS-IRO: the focal length of the lens was reported for a wavelength in the UV range, but the calibration process was done using a visible light. This means for the visible wavelengths used to illuminate the calibration pattern, the focal length of the lens was not positioned at the center of the vessel. In the future this may be remedied by using a visible-wavelength lens for calibration, or using a UV lamp to illuminate the patterned image during calibration.

Spherically expanding flames are inherently stretched, and therefore the burned, unstretched state of the flame (referred to as S_b^0) must be extrapolated from the burned,

stretched state captured in the images of the flame (referred to as S_b). This process, described by Sikes [10], is completed by plotting the time-rate-of-change of the flame radius, referred to as dr/dt, as a function of the stretch rate of the flame. A representative plot of stretch rate and dr/dt is shown in Fig. 11. The early growth of the flame is affected by the energy added to the system by the spark, and the late growth of the flame can be affected by confinement of the vessel wall. Therefore, some of the dr/dt values on either end of each data set are excluded from the calculation of laminar flame speed. These cutoffs are shown in Fig. 11 as dashed lines. The positions of the cutoffs are determined by moving them manually until the residuals of the theoretical model (blue curve in Fig. 11) are minimized, as described by Sikes [10].
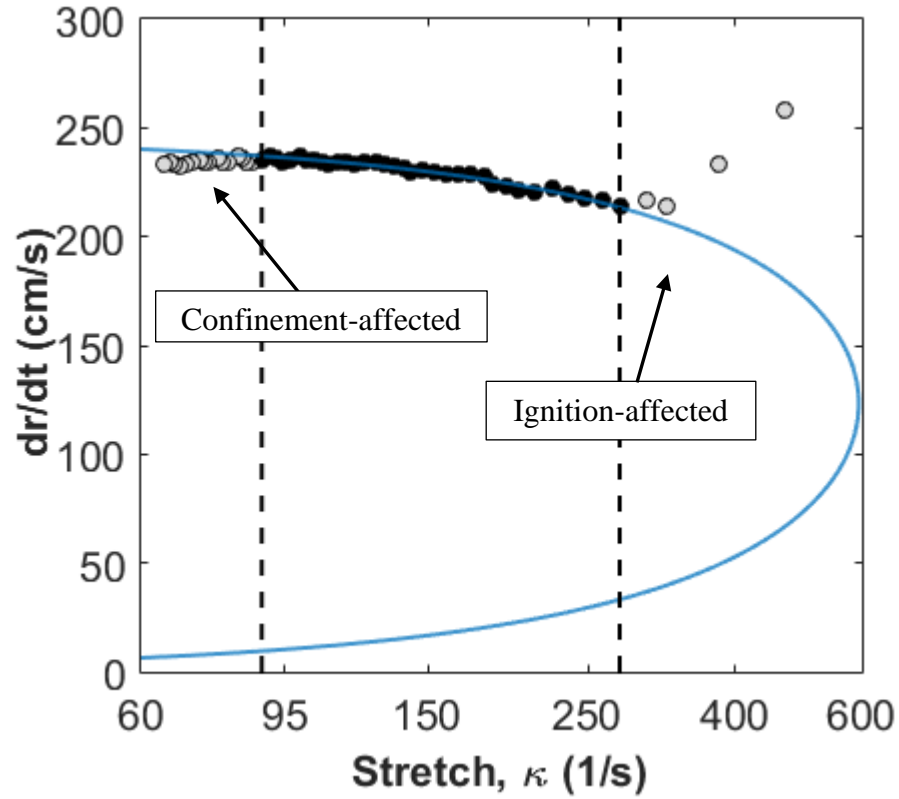
Figure 11: Example stretch plot, with a best fit of NM I to the dark points as the blue curve.

To extrapolate the burned flame speed to a condition of zero stretch, one of two non-linear methods was used, depending on the Lewis number (Le). The first non-linear method, known as NM I, was first proposed by Markstein [30] and is used when Le is greater than unity or the Markstein length is positive. NM II, proposed by Kelley [31], is used when Le is less than unity (negative Markstein length). Either method is accurate when Le is close to unity [32]. Non-linear methods NM I and NM II are included as Equations 1 and 2, respectively. The extrapolation of flame speed to zero stretch is done analytically, but graphically it can be visualized by simply finding the value of flame speed at which the upper half of the blue curve intersects the vertical axis. After

extracting burned, stretched flame speed from the data, the ratio of the densities of the burned gases (ρ_b) and the unburned gases (ρ_u) is used to convert S_b^0 to the unburned, unstretched flame speed, referred to as S_L^0. The densities of the burned gases and unburned gases are calculated using an equilibrium chemistry solver, such as the one provided in Chemkin. In Equations 1 and 2, $L_{m,b}$ refers to the burned Markstein length, and r refers to the radius of the flame. The Markstein length is determined by the best fit of the appropriate non-linear method to the data.

$$S_b = S_b^0 - S_b^0 L_{m,b} \cdot \frac{2}{r} \tag{1}$$

$$\ln(S_b) = \ln(S_b^0) - S_b^0 L_{m,b} \cdot \frac{2}{rS_b} \tag{2}$$

$$S_L^0 = S_b^0 \cdot \frac{\rho_b}{\rho_u} \tag{3}$$

5. EXPERIMENTAL RESULTS AND DISCUSSION[*]

Three sets of laminar flame speed data are reported here: first, the data from each of the three emission markers; second, the data from the simultaneous schlieren and OH* chemiluminescence tests; third, the data relating to the carbon dioxide-based flames. All the new data reported herein are also tabulated in Appendix A.

5.1. Methane-Air Flame Speed from Chemiluminescence

Figure 12 presents the new laminar flame speed data for methane at 1 atm and room temperature for each of the three emission markers—CH*, OH*, and broadband. The estimated uncertainty of the data in this work is ±5%, shown by the error bars in Fig. 12. Each of the three wavelength bandwidths produced similar flame speeds at each equivalence ratio. Therefore, all of the chemiluminescence data at each equivalence ratio were averaged to simplify the comparison with the literature data, which is plotted in Fig. 13. The new chemiluminescence method produces laminar flame speeds that agree well with established literature for every equivalence ratio tested. The literature data reproduced in Fig. 13 are taken from Aung et al. [33], Bosschart and de Goey [34], Gu et al. [35], Hassan et al. [36], Lowry et al. [5], Rozenchan et al. [37], Sikes et al. [10], Tahtouh et al. [38], and Vagelopoulos and Egolfopoulos [39]. For clarity and legibility, all of the literature data reported in Fig. 13 are displayed using the same symbol. All of

the literature data reproduced herein were measured using a spherically expanding flame apparatus, with the exception of the data reported by Bosschaart and de Goey (heat flux), and Vagelopoulos and Egolfopoulos (flat flame). The Aramco 1.3 mechanism is also plotted here for reference, and is shown to agree well with the data obtained from chemiluminescence. These results confirm the accuracy of the new chemiluminescence diagnostic.
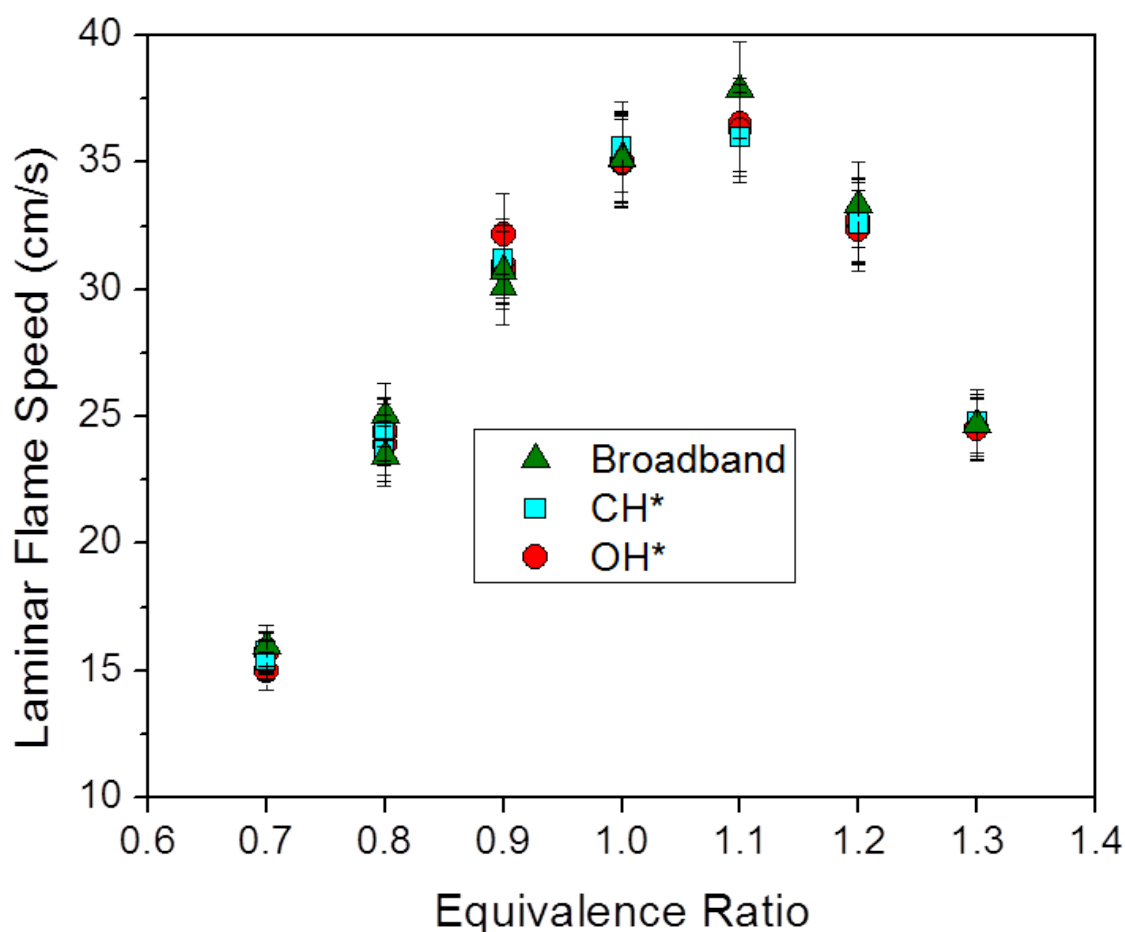
Figure 12: Laminar flame speed of methane-air measured from different wavelengths of chemiluminescence at one atmosphere and room temperature for a range of equivalence ratios.
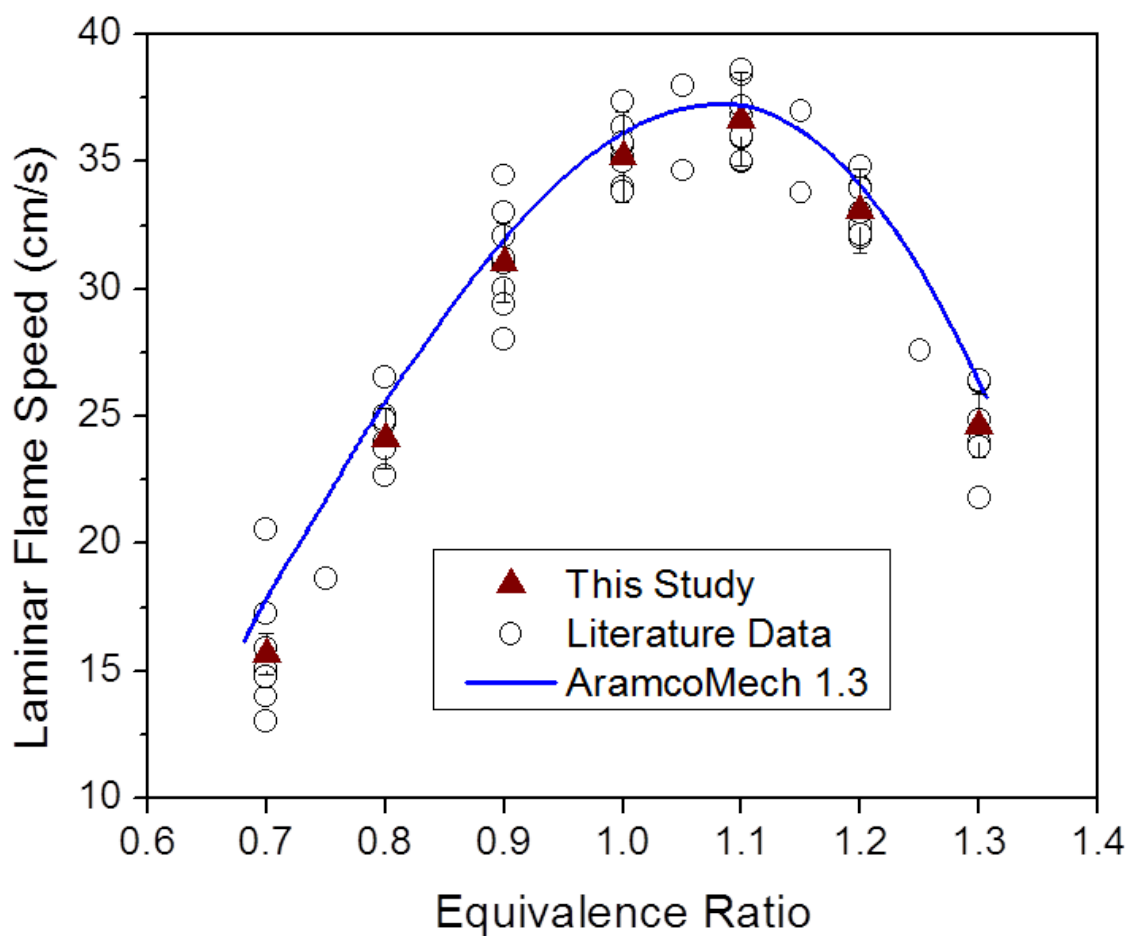
Figure 13: Averaged chemiluminescence data with error bars denoting standard deviation. Literature data and the Aramco mechanism also shown.

The images for each targeted wavelength of chemiluminescence were also compared for each equivalence ratio to determine qualitatively the differences between the types of chemiluminescence. An example of this comparison is shown in Fig. 14, where each type of chemiluminescence is compared for three timestamps at the stoichiometric equivalence ratio.
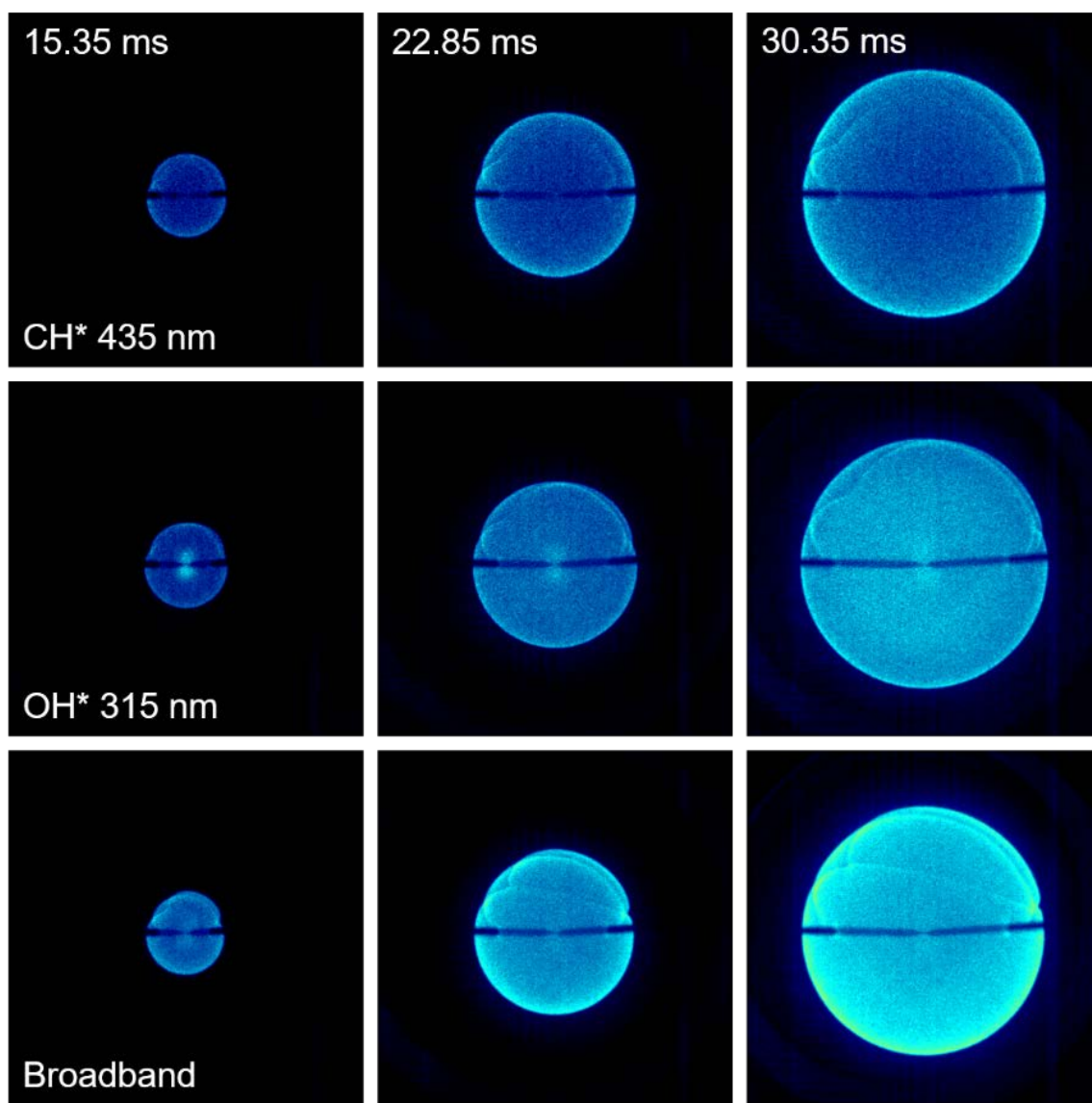
Figure 14: Images from three tests conducted at the stoichiometric equivalence ratio for the three different emission bandwidths. The time stamps correspond to each column, and the emission wavelength labels correspond to each row.

There are several differences between the types of chemiluminescence that are worth noting. First, the distribution of intensity across the flame is unique for each wavelength. The broadband emission is very bright at the edge of the flame and only

fades slightly at center of the flame, whereas the CH* chemiluminescence is much less intense at the center of the flame. The OH* emission is somewhat brighter at the leading edge of the flame than it is toward the center of the flame, and it increases in intensity in the center of the flame as the flame grows. This gradient indicates that OH* is present in the interior of the flame even after the initial flame front passes. The OH* images also exhibit artifacts of the spark for much longer than the other wavelengths. The CH* images are notable for exhibiting a clearly defined, bright leading flame edge that lends itself well to the application of the same routines used for the previously existing schlieren image processing. A higher gain was required for the CH* images as compared to the OH* and broadband images. The broadband images tended to be more likely saturated as compared to the OH* or CH* images, even with the low-gain settings. This bright intensity caused a glow to appear around the flame in many of the late-flame images, as can be seen in the 30.35-ms image of broadband chemiluminescence in Fig. 14. It is also worth noting that these chemiluminescence images capture many of the physical features of the flame that make the schlieren measurement of spherical flames visually interesting. For example, the wrinkles caused by the passing of the flame front over the electrodes are apparent in the images of each of the three types of chemiluminescence.

Because the broadband emission cannot be traced back to any single species, its utility is limited simply to laminar flame speed measurements and qualitative image analysis. For this reason, it will be more practical to select a single wavelength at which to continue this testing that can be directly related to the concentration or population of a

radical of interest, so that this type of imaging can be used for additional analysis, such as flame reaction zone thickness [28]. OH* and CH* chemiluminescence both show promise in this regard. CH* may have an advantage over OH* because of the higher contrast between the leading edge of the flame and the center of the flame and because of the lack of residual spark emission in the CH* images.

5.2. Simultaneous OH* Chemiluminescence and Schlieren Imaging

The resulting laminar flame speed data from the simultaneous imaging of schlieren and OH* chemiluminescence are plotted alongside the Aramco 1.3 mechanism in Fig. 15. Again, methane-air mixtures were used at equivalence ratios of 0.7 to 1.3, every 0.1. Uncertainty bars are included here for both schlieren and chemiluminescence points. For the schlieren, the uncertainty is on the order of 1% [10]. The chemiluminescence data have the same 5% uncertainty as before. There is good agreement between the model and the data, and between the schlieren-derived measurements and the chemiluminescence-derived measurements. Within the uncertainty, the two measurements are indistinguishable. That being said, the uncertainty of the chemiluminescence measurement can be improved by increasing the quality of the calibration images, as described previously in Chapter 4.
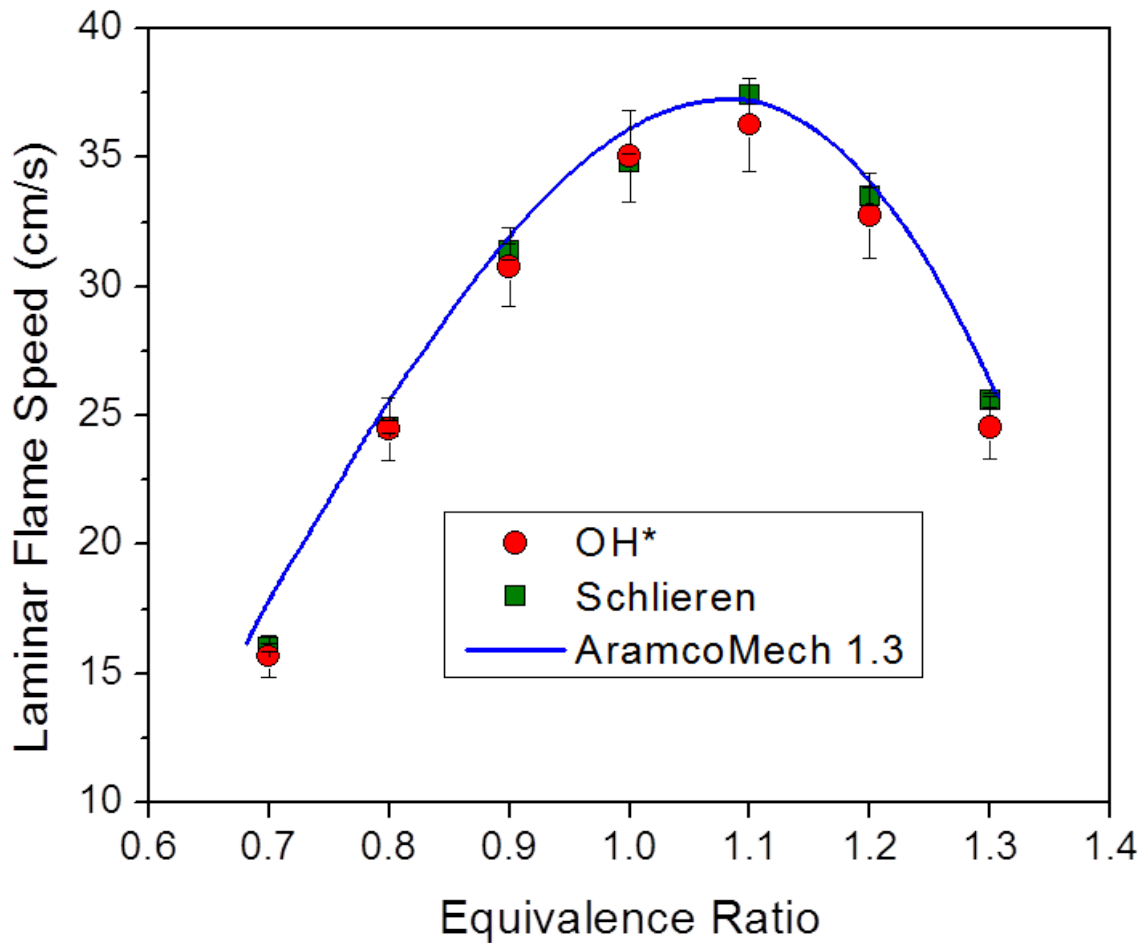
Figure 15: Comparison of chemiluminescence- and schlieren-derived flame speed.

The direct comparison of the two optical diagnostics also revealed an interesting event in one of the experiments: for the test at an equivalence ratio of 1.1, a secondary event occurred after the initial spark ignition event. This type of event had not been seen in any previous experiments and has yet to be observed again in the author's experience. The cause of this event is unknown, but the event caused the flame to grow unevenly, producing wrinkles and a region that deviated from the main flame sphere. The schlieren images and chemiluminescence images are shown side by side in Fig. 16. All of this

behavior was captured by the chemiluminescence diagnostic, as shown by the red features in Fig. 16. The schlieren images picked up some of the wrinkles and a hint of the deviated region, but otherwise seemed normal. This event was captured partly because of the difference in the physical perspective of the two imaging setups, but also because the chemiluminescence diagnostic can register such chemically reactive events. This type of feature is another reason to use a chemiluminescence diagnostic for these spherically expanding flame tests.
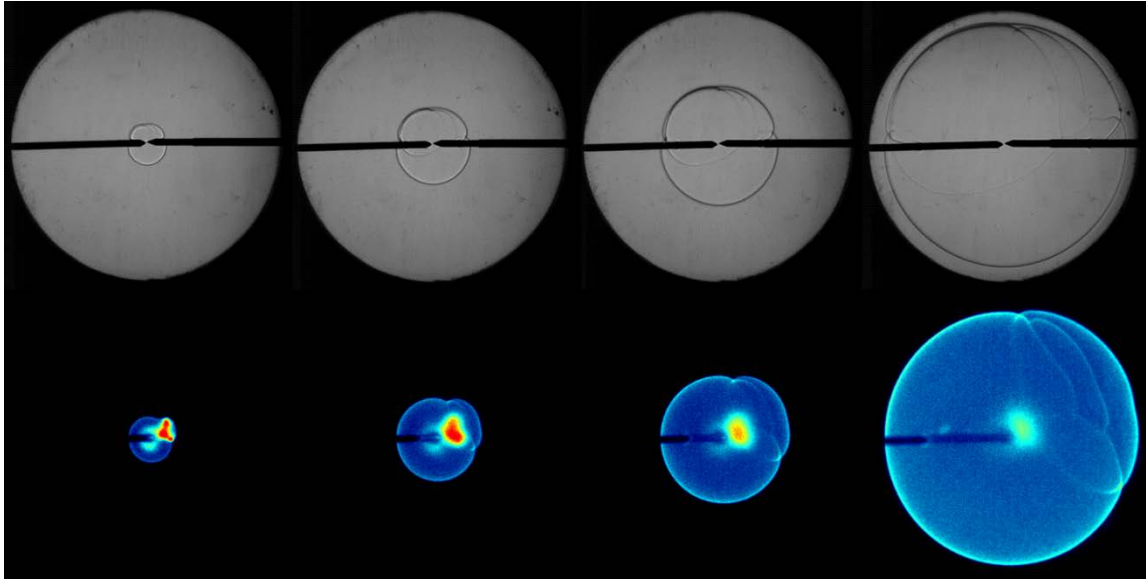
Figure 16: Simultaneous schlieren and chemiluminescence imaging of a methane-air flame at phi=1.1, room temperature, and one atmosphere.

5.3. Methane-Oxygen-Carbon Dioxide Laminar and Turbulent Results

This section details the approach for the CO_2-based flame tests and then discusses the laminar data and the turbulent data separately. All of the CO_2-based flame tests were imaged using OH* chemiluminescence. The initial test matrix was chosen to

provide a standardized metric of comparison between the flame speeds of these CO_2-based flames and the flame speeds of air-based flames. The molar ratio of O_2 to CO_2 in the oxidizer mixture was initially chosen such that the adiabatic flame temperatures of the CO_2-based methane flames would closely match the adiabatic flame temperatures of air-based methane flames for the relevant range of equivalence ratios. This criterion produced an oxidizer mixture of 31% O_2 and 69% CO_2. However, upon testing these flames, it was found that the flame propagation was too slow to overcome the effect of buoyancy on the flame. Figure 17 shows the progression of one such flame, where the burned gas is floating upward faster than the reaction is propagating downward, causing the flame to grow toward the top of the vessel much more quickly than toward the bottom.
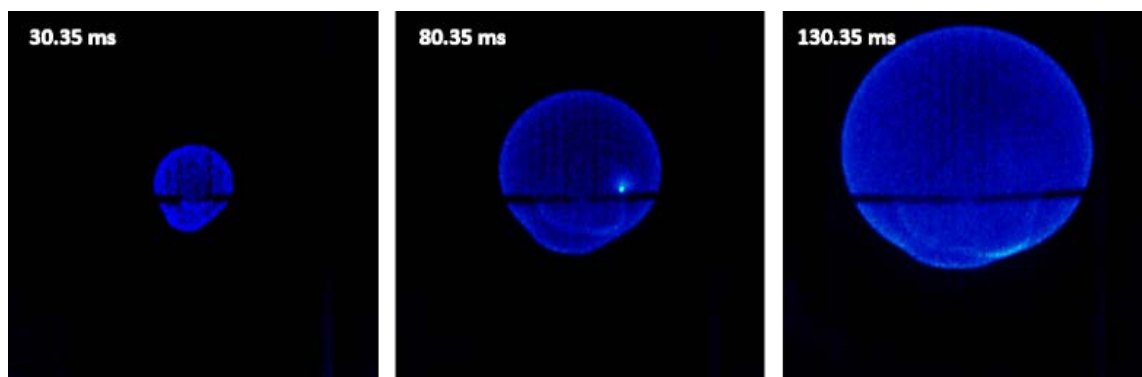
Figure 17: Progression of buoyant CH_4-O_2-CO_2 flame at an equivalence ratio of 0.7 and a relative O_2 concentration in the oxidizer mixture of 31%. The bright spot in the middle frame is likely a burning dust particle, not a feature of the flame.

To overcome the effect of buoyancy on the flames, and therefore to allow buoyancy to be neglected in the analysis of these images, the concentration of O_2 in the

oxidizer mixture was increased until the flame front propagated faster than the burned gas floated. This O_2 concentration was found to be approximately 34%. As shown in Fig. 18, the effects of buoyancy are only slightly apparent during the late flame for this mixture. These diagnostic tests were run at an equivalence ratio of 0.7, which corresponds to the lowest flame speed of the range of equivalence ratios tested in this study, and therefore represents the condition at which buoyancy will be the most apparent for this study. For all other equivalence ratios tested at this O_2 concentration, the flame speed was high enough that buoyancy was not observed in any of the flames at any point.
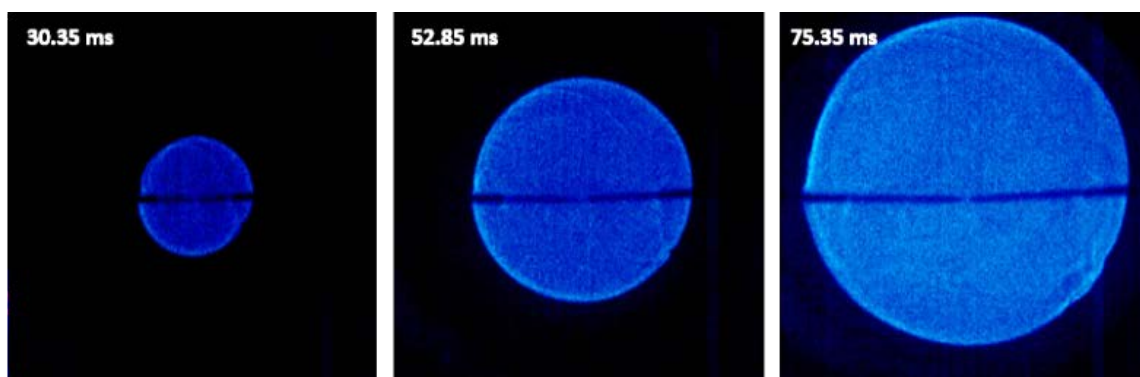
Figure 18: Progression of CH_4-O_2-CO_2 flame at an equivalence ratio of 0.7 and a relative O_2 concentration in the oxidizer mixture of 34%. Buoyancy is minor.

The adiabatic flame temperature of each equivalence ratio for the new 34% O_2 mixture was then calculated, and they were all found to be higher than the flame temperatures of the previous 31% O_2 mixture by approximately 100 K for the full range of equivalence ratios. The adiabatic flame temperatures of both CO_2-based mixtures and of the air-based mixture are plotted for comparison in Fig. 19.
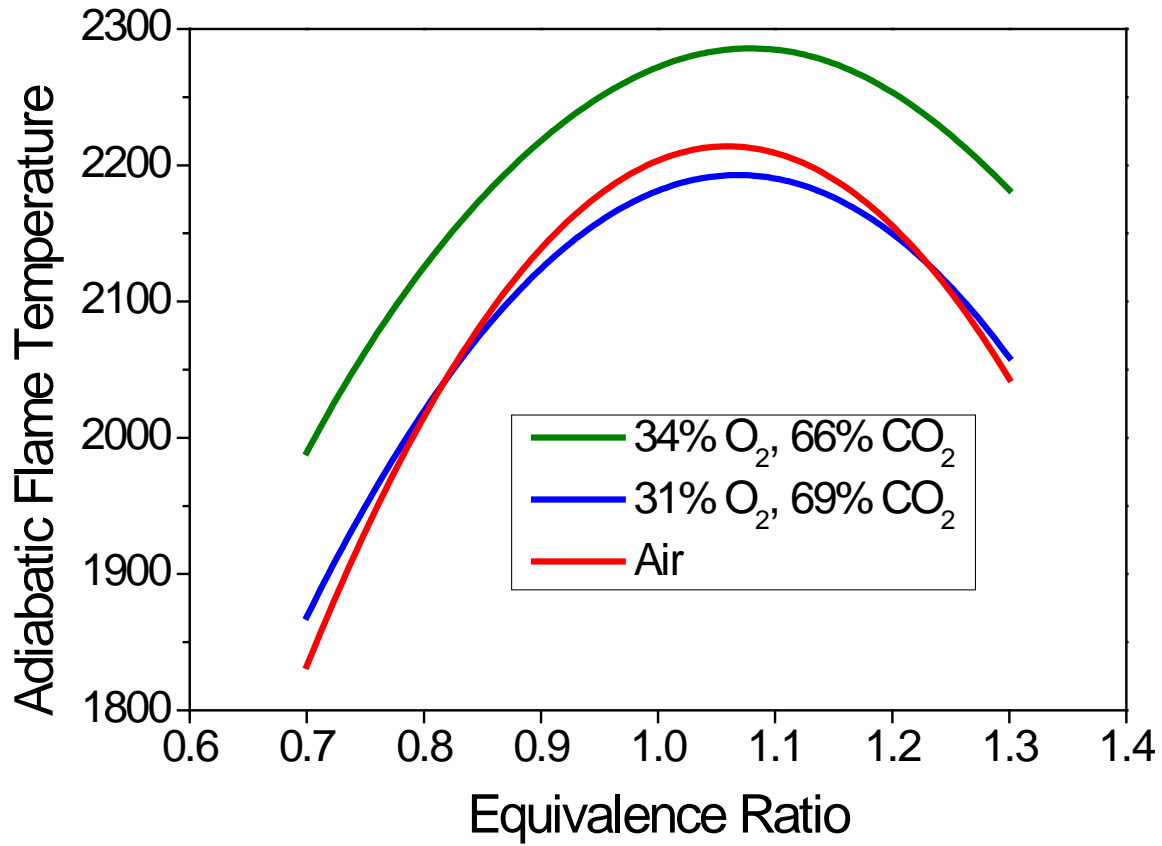
Figure 19: Adiabatic flame temperatures for three methane-oxidizer mixtures for a range of equivalence ratios.

5.3.1. Laminar CO₂-Based Flame Data

Figure 20 plots the measured laminar flame speeds of the CH_4-O_2-CO_2 flames from this study, as well as data in the literature from Khan et al. [40] and Hu et al. [41] for 1 atm and 300 K. There are additional data for CH_4-O_2-CO_2 flames reported by Xie et al. [42], Konnov and Dyakov [43], and Hu et al. [44], but for simplicity and legibility those data are not reproduced here. The new data are in good agreement with the flame speeds reported by Hu et al. [41]. For each equivalence ratio except stoichiometric, the flame speed of the 34% O_2 flames is between the values reported by Hu et al. [41] for 33% and 35% O_2. A peak flame speed of 24.8 cm/s is reached at the stoichiometric

equivalence ratio, while the equivalence ratio of 0.7 produced the lowest flame speed of 15.2 cm/s. At an elevated initial pressure of 5 atm and at the stoichiometric equivalence ratio, a laminar flame speed of 13.25 m/s was measured, representing a 46.5% decrease. The uncertainty in the measured flame speeds in this work, due to repeatability of the experiments, gas mixture temperatures, gas mixture compositions, model fit, and solution methods, is estimated to be ±5%.
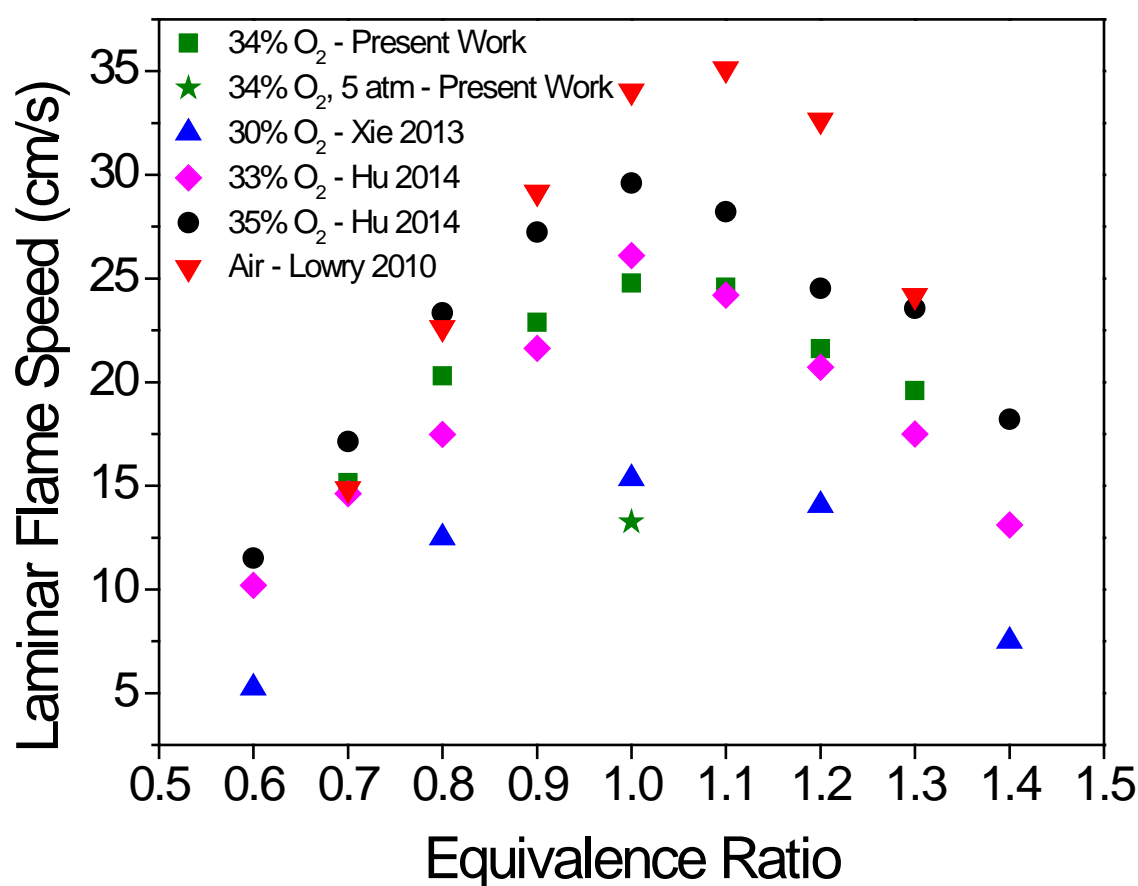
Figure 20: Laminar flame speed of CH₄-O₂-CO₂ flames of various O₂ concentrations, with a set of CH₄-air flame speeds included for comparison. All data are for initial conditions of 1 atm and 300 K, except the 5-atm point represented by a star.

Even though the calculated adiabatic flame temperatures of the 34% O_2 flames are much higher than those of the CH_4-air flames, the flame speeds of the 34%-O_2-based flames are significantly lower than those of the air-based flames, with the exception of the equivalence ratio of 0.7, where the flame speeds of the air-based flames and the CO_2-based flames are very close to each other. This trend indicates that CO_2 has a significant chemical effect beyond the thermodynamic effect of the increased heat capacity, as reported in [44]. Carbon dioxide participates in the $OH + CO \rightleftarrows H + CO_2$ reaction in reverse, impeding the combustion process by removing H radicals [42, 44].

Figure 21 tracks the growth of a 1-atm stoichiometric, laminar CH_4-O_2-CO_2 flame at an O_2 concentration of 34%. As in Figs. 14 and 18, the leading edge of the flame is crisp and easily differentiable from the surrounding unburned gas. There is some scattering of light in Fig. 21 in the unburned gas as the flame grows and brightens, causing a glow to appear throughout the image. This noise can be decreased by decreasing the gain of the intensifier, but it cannot be completely avoided without sacrificing the usefulness of the darker images at the beginning of flame growth. Physical features of the flame are also faintly visible in Fig. 21, although Fig. 16 is a better example of this. A few wrinkles, caused by the interaction of the flame with the electrodes, can be followed throughout the growth of the flame. This type of feature is readily visible in typical schlieren images of spherically expanding flames, and this chemiluminescence diagnostic proves capable of capturing similar details. However, future work will fine-tune the optics to capture a higher level of detail, and it may be appropriate to target a different radical known to emit at a lower intensity, like CH*.
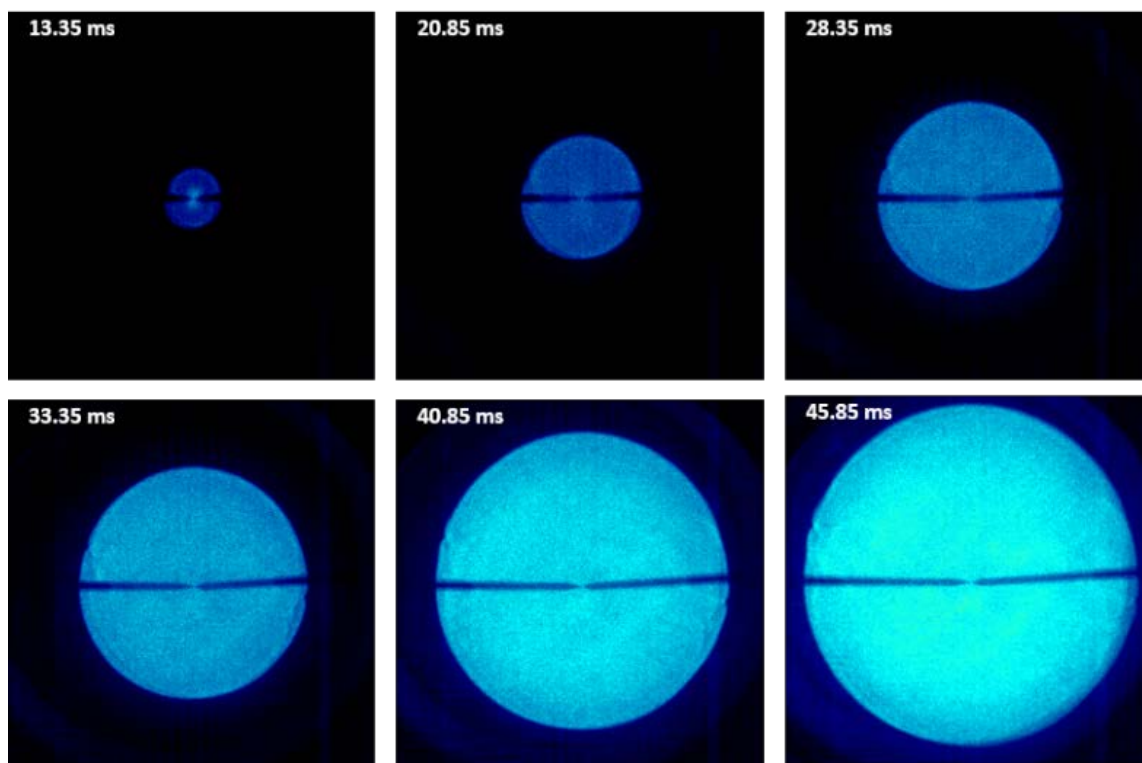
Figure 21: Progression of a 1-atm CH$_4$-O$_2$-CO$_2$ flame at an equivalence ratio of 1.0 and a relative O$_2$ concentration of 34%.

Images of chemiluminescence of a CH$_4$-O$_2$-CO$_2$ flame at an initial pressure of 5 atm are shown in Fig. 22. At higher pressures, thermal-diffusive instabilities develop earlier in the growth of the flame. These instabilities can be seen developing at the leading edge of the flame in the bottom three frames of Fig. 22. As these instabilities do not reflect purely laminar flame behavior, the frames were not used in the measurement of laminar flame speed for this condition.

Because the chemiluminescence diagnostic employed in this study captures a two-dimensional projection of the flame, the center of the flame in these images begins to lose clarity as the flame grows, and the edge of the flame becomes softer. In contrast,

42

the edges of the 1-atm flames are crisp and bright, as in Figs. 2, 9, 14, 16, and 21. The thermal-diffusive instabilities are encouraged by the elevated pressure, which causes the reaction zone of the flame to spread out and produces the soft edges seen in Fig. 22.
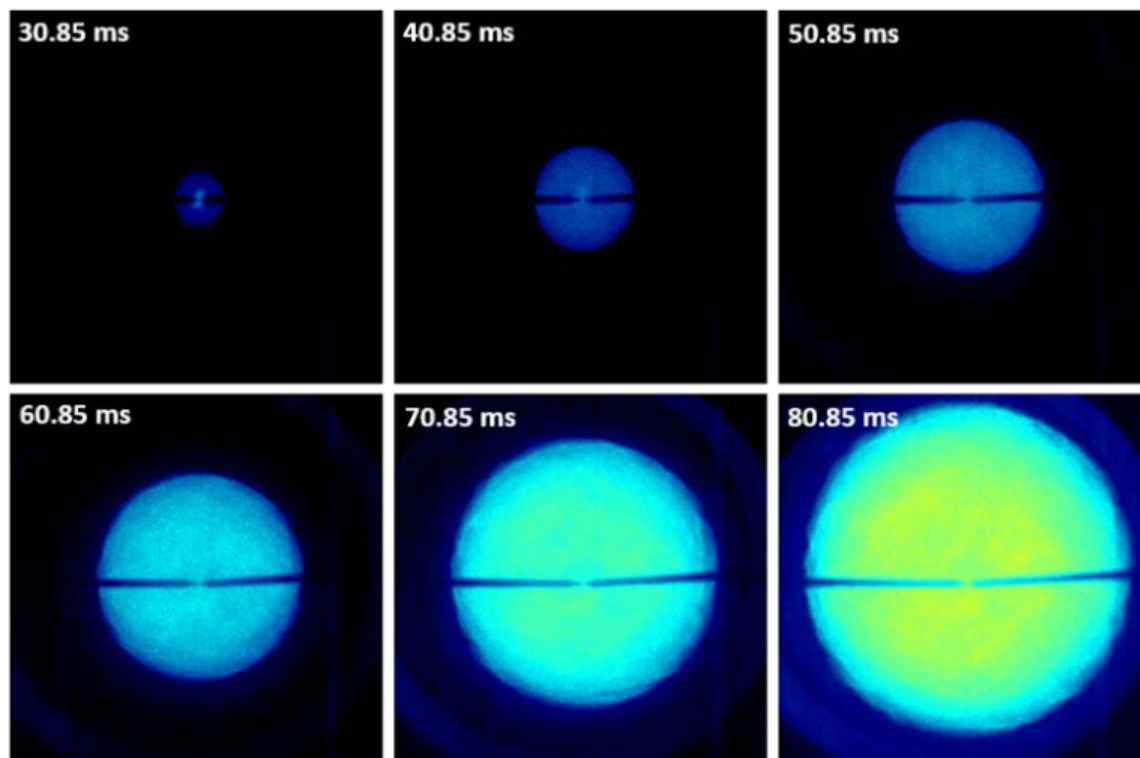
Figure 22: Progression of a quiescent CH_4-O_2-CO_2 flame at stoichiometric equivalence ratio and 5-atm initial pressure.

Improvements in this area can be done to further improve image quality. Image quality in the present context refers to the images of the flame, not the calibration images mentioned previously. For analysis of flame features such as wrinkling, cellularity, and thermal-diffusive instabilities, decreasing the gain of the intensifier would help clear up the late-flame images but would negatively affect the early-flame images. These early

flame images will be darker, but they can then be brightened during analysis to glean further information from them. Decreasing the gain will also help minimize the noise in the image caused by scattering and diffraction, which is especially visible in the last frame of Fig. 22.

5.3.2. Turbulent CO_2-Based Flame Data

For the turbulent flame tests, the recording rate of the camera and intensifier was increased to 8000 frames per second to account for the increased rate of flame propagation. The gate width of each frame was not changed. Two tests at initial conditions of 1 atm, 300 K, and stoichiometric equivalence ratio were performed. For all turbulent tests in this study, the stirring motors were set to 2000 rpm. The speed of each motor was measured using a stroboscope. The turbulence generated by this combination of motor speed and impellers has been characterized previously using laser Doppler velocimetry [12, 14]. The root mean square turbulence fluctuation for these impellers at 2000 rpm was found to be approximately 1.4 m/s. Modelling of turbulent flame behavior is an active field of research but was not performed for this study. A qualitative analysis of the turbulent flame images recorded for this study is presented here.

Images from two individual turbulent flame tests are presented in Fig. 23. For the turbulent flame tests, the emission caused by the spark persists throughout the duration of the experiment. Note the time stamps of Fig. 23 in comparison to the time stamps of Figs. 14, 21, and 22. For the laminar cases, the flame speed is slow enough that the spark emission decays well before the flame has grown beyond the aperture of the window.

For the turbulent cases, the flame grows to the edge of the viewable region well before the spark has decayed. For both sets of turbulent images, this region of the spark-affected flame can be visually tracked as it drifts slightly right-of-center.

There are some minor differences in the shape of the flame between the two turbulent tests, which are to be expected due to the chaotic nature of turbulent flow. In both tests, the flame is approximately symmetric with respect to the center of the flame, indicating a near-symmetric flow field. However, the leading edge of the flame is not as clear as in the laminar tests, and the center of the flame begins to lose definition in the late-flame images, similar to the images of the quiescent, 5-atm condition.

To increase image quality for turbulent flames, where the flame growth rate is much higher than for laminar flames, the exposure time of each frame can be decreased. This decrease in exposure time will lower the amount of emission gathered by the camera sensor in each frame, requiring an increase in the intensifier gain, but it will also decrease the distance that the flame grows during the exposure time of each image. This result will increase image clarity and decrease the blur at the edge of flame. This change will not have a pronounced effect on slower, i.e. laminar, flames, but it will require an increase in the gain value. Chemiluminescence imaging of CH* in turbulent flames may also produce a greater level of detail, as mentioned for laminar flames.
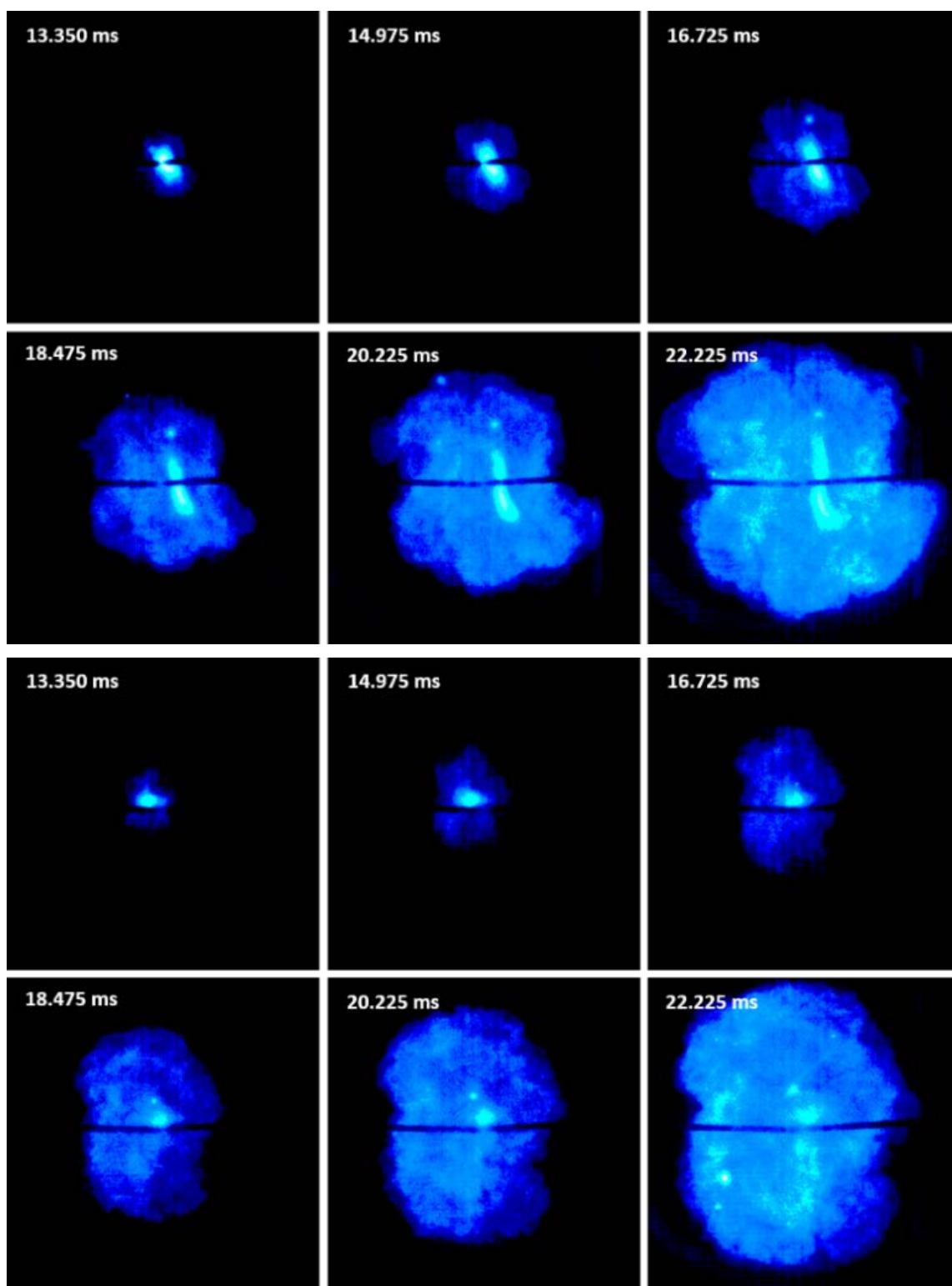
Figure 23: Progression of two different runs of turbulent CH_4-O_2-CO_2 flames at 1 atm, 298 K, stoichiometric equivalence ratio, and turbulence fluctuation of 1.4 m/s.

6. CONCLUSIONS AND FUTURE WORK

Chemiluminescence imaging can produce detailed images of spherical flames; from these images, laminar flame speed and more can be extracted, but additional work can improve the technique and the associated uncertainty. The range of intensity at 306 nm produced by these CO_2-diluted flames requires more careful tuning of the gain of the intensifier optics, so that late-flame images can be more informative. Laminar flame speeds of methane-air flames measured from chemiluminescence agree well with the established spherical-flame literature data, which has been traditionally recorded by schlieren photography. The method also provides laminar flame speed data for carbon-dioxide-based flames that agree very well with reported values. Simultaneous imaging of schlieren and chemiluminescence showed no significant difference between the flame speeds derived from each method. This work validates chemiluminescence as a method by which to measure laminar flame speed from spherically expanding flames.

Nonetheless, this chemiluminescence diagnostic has some room for improvement for imaging turbulent flames in this application. Currently, the images of OH* emission from turbulent flames are not clear enough to provide better information than schlieren imaging does already. The gate width of the intensifier can be decreased and the frame rate increased to capture the fast turbulent flame dynamics.

Carbon dioxide as a diluent affects flame speed beyond what is predicted from calculations of adiabatic flame temperature, indicating that it may participate in the combustion chemistry. The next step in this direction involves more investigation of the

high-pressure and high-temperature behavior of oxy-methane-CO_2 flames, both laminar and turbulent, to satisfy the need for further understanding of supercritical carbon dioxide combustors.

REFERENCES

[1] S.R. Turns. An Introduction to Combustion: Concepts and Applications. 3 ed., McGraw-Hill, New York, 2012.

[2] K. Annamalai, I.K. Puri. Combustion Science and Engineering. CRC Press, Boca Raton, FL, 2007.

[3] F.A. Williams. Combustion Theory: The Fundamental Theory of Chemically Reacting Flow Systems. 2 ed., CRC Press, Boca Raton, FL, 1985.

[4] J. de Vries. A study on spherical expanding flame speeds of methane, ethane, and methane/ethane mixtures at elevated pressures. PhD dissertation, Mechanical Engineering, Texas A&M University, College Station, 2009.

[5] W. Lowry, J. de Vries, M. Krejci, E.L. Petersen, Z. Serinyel, W. Metcalfe, H. Curran, G. Bourque. Laminar Flame Speed Measurements and Modeling of Pure Alkanes and Alkane Blends at Elevated Pressures. ASME Turbo Expo, 2010, Glasgow, UK: American Society of Mechanical Engineers. pp.855-873.

[6] J. de Vries, W.B. Lowry, Z. Serinyel, H.J. Curran, E.L. Petersen. Laminar flame speed measurements of dimethyl ether in air at pressures up to 10 atm. Fuel 90 (2011) 331-338.

[7] M.C. Krejci, O. Mathieu, A.J. Vissotski, S. Ravi, T.G. Sikes, E.L. Petersen, A. Kérmonès, W. Metcalfe, H.J. Curran. Laminar Flame Speed and Ignition Delay Time Data for the Kinetic Modeling of Hydrogen and Syngas Fuel Blends. Journal of Engineering for Gas Turbines and Power 135 (2013) 021503-021509.

[8] S. Ravi, T.G. Sikes, A. Morones, C.L. Keesee, E.L. Petersen. Comparative study on the laminar flame speed enhancement of methane with ethane and ethylene addition. Proc. Combust. Inst. 35 (2015) 679-686.

[9] T. Sikes, M.S. Mannan, E.L. Petersen. Laminar flame speeds of nano-aluminum/methane hybrid mixtures. Combust. Flame 166 (2016) 284-294.

[10] T. Sikes, M.S. Mannan, E.L. Petersen. An experimental study: laminar flame speed sensitivity from spherical flames in stoichiometric CH_4–air mixtures. Combust. Sci. Tech. 190 (2018) 1594-1613.

[11] A. Morones, V.J. Leon, E.L. Petersen. Reconfigurable Fan-Stirred Flame Bomb with Optical Access. 55th AIAA Aerospace Sciences Meeting, 2017, Grapevine, TX: American Institute of Aeronautics and Astronautics.

[12] A. Morones, M.A. Turner, V.J. Leon, K. Ruehle, E.L. Petersen. Validation of a New Turbulent Flame Speed Facility for the Study of Gas Turbine Fuel Blends at Elevated Pressure. ASME Turbo Expo, 2019, Phoenix, AZ: American Society of Mechanical Engineers.

[13] S. Ravi, A. Ruelas, E. Petersen. Measurement of Turbulent Flame Propagation Rates of Methane Using a New Facility. 51st AIAA Aerospace Sciences Meeting, 2013, Grapevine, TX. pp.1184.

[14] A. Morones. Study of spherical turbulent flames in a reconfigurable fan-stirred bomb. PhD dissertation, Mechanical Engineering, Texas A&M University, College Station, 2018.

[15] D.S. Dandy, S.R. Vosen. Numerical and Experimental Studies of Hydroxyl Radical Chemiluminescence in Methane-Air Flames. Combust. Sci. Tech. 82 (1992) 131-150.

[16] C. Xiouris, T. Ye, J. Jayachandran, F.N. Egolfopoulos. Laminar flame speeds under engine-relevant conditions: uncertainty quantification and minimization in spherically expanding flame experiments. Combust. Flame 163 (2016) 270-283.

[17] G.S. Settles. Schlieren and shadowgraph techniques: visualizing phenomena in transparent media. Springer Science & Business Media, 2012.

[18] E.K. Rideal. Chemiluminescence. Nature 123 (1929) 417-419.

[19] W.E. Garner, K. Tawada. The radiation from the hydrogen-oxygen flame. Transactions of the Faraday Society 26 (1930) 36-45.

[20] H.A. Beatty, G. Edgar. The Vapor-phase Oxidation of Hydrocarbons and Chemiluminescence of n-Heptane. Journal of the American Chemical Society 56 (1934) 112-114.

[21] F.V. Tinaut, M. Reyes, B. Giménez, J.V. Pastor. Measurements of OH* and CH* chemiluminescence in premixed flames in a constant volume combustion bomb under autoignition conditions. Energy & Fuels 25 (2010) 119-129.

[22] J. Kojima, Y. Ikeda, T. Nakajima. Spatially resolved measurement of OH*, CH*, and C_2* chemiluminescence in the reaction zone of laminar methane/air premixed flames. Proc. Combust. Inst. 28 (2000) 1757-1764.

[23] Y. Ikeda, M. Kaneko, T. Nakajima. Local A/F Measurement by Chemiluminescence OH*, CH* and C_2* in SI Engine. SAE Transactions 110 (2001) 754-760.

[24] C.S. Panoutsos, Y. Hardalupas, A. Taylor. Numerical evaluation of equivalence ratio measurement using OH* and CH* chemiluminescence in premixed and non-premixed methane–air flames. Combust. Flame 156 (2009) 273-291.

[25] V. Nori, J. Seitzman. Evaluation of chemiluminescence as a combustion diagnostic under varying operating conditions. 46th AIAA Aerospace Sciences Meeting and Exhibit, 2008, Reno, Nevada: AIAA. pp.953.

[26] Y. Hardalupas, M. Orain. Local measurements of the time-dependent heat release rate and equivalence ratio using chemiluminescent emission from a flame. Combust. Flame 139 (2004) 188-207.

[27] M.A. Turner, T. Paschal, P. Parajuli, W.D. Kulatilaka, E.L. Petersen. Laminar Flame Speed Measurements from Chemiluminescence of OH* and CH* in CH_4-Air Flames. AIAA SciTech Forum, 2019, San Diego, CA: American Institute of Aeronautics and Astronautics, Inc.

[28] T. Paschal, P. Parajuli, M.A. Turner, E.L. Petersen, W.D. Kulatilaka. High-Speed OH* and CH* Chemiluminescence Imaging and OH Planar Laser-Induced Fluorescence (PLIF) in Spherically Expanding Flames. AIAA SciTech Forum, 2019, San Diego, CA: American Institute of Aeronautics and Astronautics, Inc.

[29] J. Canny. A computational approach to edge detection. IEEE Transactions on Pattern Analysis and Machine Intelligence 8 (1986) 679-698.

[30] G.H. Markstein. Experimental and theoretical studies of flame-front stability. Journal of the Aeronautical Sciences 18 (1951) 199-209.

[31] A.P. Kelley, C.K. Law. Nonlinear effects in the extraction of laminar flame speeds from expanding spherical flames. Combust. Flame 156 (2009) 1844-1851.

[32] Z. Chen. On the extraction of laminar flame speed and Markstein length from outwardly propagating spherical flames. Combust. Flame 158 (2011) 291-300.

[33] K.T. Aung, L.K. Tseng, M.A. Ismail, G.M. Faeth. Response to comment by S.C. Taylor and D.B. Smith on "laminar burning velocities and Markstein numbers of hydrocarbon/air flames". Combust. Flame 102 (1995) 526-530.

[34] K.J. Bosschaart, L.P.H. de Goey. The laminar burning velocity of flames propagating in mixtures of hydrocarbons and air measured with the heat flux method. Combust. Flame 136 (2004) 261-269.

[35] X.J. Gu, M.Z. Haq, M. Lawes, R. Woolley. Laminar burning velocity and Markstein lengths of methane–air mixtures. Combust. Flame 121 (2000) 41-58.

[36] M.I. Hassan, K.T. Aung, G.M. Faeth. Measured and predicted properties of laminar premixed methane/air flames at various pressures. Combust. Flame 115 (1998) 539-550.

[37] G. Rozenchan, D.L. Zhu, C.K. Law, S.D. Tse. Outward propagation, burning velocities, and chemical effects of methane flames up to 60 atm. Proc. Combust. Inst. 29 (2002) 1461-1470.

[38] T. Tahtouh, F. Halter, C. Mounaïm-Rousselle. Measurement of laminar burning speeds and Markstein lengths using a novel methodology. Combust. Flame 156 (2009) 1735-1743.

[39] C.M. Vagelopoulos, F.N. Egolfopoulos. Direct experimental determination of laminar flame speeds. Symp. (Int.) Combust. 27 (1998) 513-519.

[40] A.R. Khan, S. Anbusaravanan, L. Kalathi, R. Velamati, C. Prathap. Investigation of dilution effect with N_2/CO_2 on laminar burning velocity of premixed methane/oxygen mixtures using freely expanding spherical flames. Fuel 196 (2017) 225-232.

[41] X. Hu, Q. Yu, J. Liu, N. Sun. Investigation of laminar flame speeds of $CH_4/O_2/CO_2$ mixtures at ordinary pressure and kinetic simulation. Energy 70 (2014) 626-634.

[42] Y. Xie, J. Wang, M. Zhang, J. Gong, W. Jin, Z. Huang. Experimental and Numerical Study on Laminar Flame Characteristics of Methane Oxy-fuel Mixtures Highly Diluted with CO_2. Energy & Fuels 27 (2013) 6231-6237.

[43] A.A. Konnov, I.V. Dyakov. Measurement of propagation speeds in adiabatic cellular premixed flames of $CH_4+O_2+CO_2$. Experimental Thermal and Fluid Science 29 (2005) 901-907.

[44] X. Hu, Q. Yu, J. Liu. Chemical effect of CO_2 on the laminar flame speeds of oxy-methane mixtures in the condition of various equivalence ratios and oxygen concentrations. International Journal of Hydrogen Energy 41 (2016) 15068-15077.

APPENDIX A

TABULATED LAMINAR FLAME SPEED DATA

Table A1: Laminar flame speeds of methane-air flames at room temperature and atmospheric pressure.

ϕ	CH* (cm/s)	OH* (cm/s)	Broadband (cm/s)	Average (cm/s)
0.7	15.5 15.7 15.4	15.0 15.7	16.0	15.7
0.8	24.5 23.6	23.9 24.3	23.4 25.1	24.1
0.9	31.0 31.2	32.2 31.0	30.1 30.7	31.0
1	35.2 35.6	35.0 35.0	35.2 35.1	35.2
1.1	36.0	36.3 36.5	37.8	36.7
1.2	32.6	32.3 32.7	33.3	33.1
1.3	24.8	24.5	24.7	24.7

Table A2: Comparison of laminar flame speeds obtained using two different optical methods for methane-air flames at room temperature and atmospheric pressure.

ϕ	OH* (cm/s)	Schlieren (cm/s)
0.7	15.7	16.0
0.8	24.5	24.6
0.9	30.8	31.4
1.0	35.0	34.8
1.1	36.3	37.4
1.2	32.7	33.5
1.3	24.5	25.6

Table A3: Laminar flame speeds of CO_2-O_2-CH_4 flames at one atmosphere and 5 atmospheres. The relative ratio of CO_2-O_2 is 66%-34%.

ϕ	1 atm (cm/s)	5 atm (cm/s)
0.7	15.2	--
0.8	20.3	--
0.9	22.9	--
1.0	24.8	13.3
1.1	24.6	--
1.2	21.6	--
1.3	19.6	--